

# **Suction feeding biomechanics of *Polypterus bichir*: investigating linkage mechanisms and the contributions of cranial kinesis to oral cavity volume change**

KATRINA R. WHITLOW<sup>1</sup>, CALLUM F. ROSS<sup>1</sup>, NICHOLAS J. GIDMARK<sup>2</sup>, J.D. LAURENCE-CHASEN<sup>1</sup>,  
MARK W. WESTNEAT<sup>1</sup>

1. *Department of Organismal Biology and Anatomy, University of Chicago, Chicago, IL 60637, USA*
2. *Department of Biology, Knox College, Galesburg, IL 61401, USA*

Keywords: *Polypterus*, suction feeding, biomechanics, volume, endocast, XROMM

Corresponding Author Information: Katrina R. Whitlow

1025 E 57<sup>th</sup> St, Culver 105, Westneat Lab

Email: kwhitlow@uchicago.edu

## **SUMMARY STATEMENT**

A kinematic analysis of feeding in *Polypterus bichir*, quantification of the relative contributions of cranial kinesis to volume change in the oral cavity, and investigation of mechanics driving cranial expansion.

## **ABSTRACT**

Many fishes use substantial cranial kinesis to rapidly increase buccal cavity volume, pulling prey into the mouth via suction feeding. Living polypterids are a key lineage for understanding the evolution and biomechanics of suction feeding due to their phylogenetic position and unique

morphology. *Polypterus bichir* have fewer mobile cranial elements compared to teleosts (e.g., immobile [pre]maxillae) but successfully generate suction through dorsal, ventral, and lateral oral cavity expansion. However, the relative contributions of these motions to suction feeding success have not been quantified. Additionally, extensive body musculature and lack of opercular jaw opening linkages make *P. bichir* of interest for examining the role of cranial vs. axial muscles in driving mandibular depression. Here we analyze the kinematics of buccal expansion during suction feeding in *P. bichir* using X-Ray Reconstruction of Moving Morphology (XROMM) and quantify the contributions of skeletal elements to oral cavity volume expansion and prey capture. Mouth gape peaks early in the strike, followed by maximum cleithral and ceratohyal rotations, and finally by opercular and suspensorial abductions, maintaining the anterior-to-posterior movement of water. Using a new method of quantifying bones' relative contributions to volume change (RCVC) we demonstrate that ceratohyal kinematics are the most significant drivers of oral cavity volume change. All measured cranial bone motions, except abduction of the suspensorium, are correlated with prey motion. Lastly, cleithral retraction is largely concurrent with ceratohyal retraction and jaw depression while the sternohyoideus maintains constant length, suggesting a central role of the axial muscles, cleithrum, and ceratohyal in ventral expansion.

## INTRODUCTION

Suction feeding - rapid oral cavity expansion that draws prey into the mouth - is considered to be the ancestral feeding mode for osteichthyan fishes (Jacobs and Holzman, 2018; Lauder, 1985). Most prior research on suction feeding mechanics has focused on derived teleosts with highly mobile skulls and numerous mechanisms for cranial expansion and successful

suction feeding. For instance, teleosts share two mechanisms for jaw depression, one driven by pectoral girdle and hyoid mobility (a mechanism common to actinopterygian fishes) and one driven by opercular mobility (thought to exist only in teleosts and *Amia*) (Camp and Brainerd, 2015; Lauder, 1980). Furthermore, many studies highlight protrusible jaws, which bring the oral jaws closer to the prey, focus suction forces more directly at the prey, and increase the rate and magnitude of forces imparted to the water bolus by increasing volumetric expansion of the buccal cavity (Alexander, 1967; Kane and Higham, 2014; Lauder, 1982; Liem, 1980; Westneat and Wainwright, 1989). However, not all cranial skeletal elements show the same degree of mobility in all suction feeding species, and the relative importance of each bone's kinematics for generating suction forces is unknown. Here we examine suction feeding in polypterid fishes, the most rootward living actinopterygian fish, which are thought to have a relatively simplified feeding system with no (pre)maxillary protrusion and a single mechanism of jaw depression (Lauder, 1980). Despite this reduced cranial mobility, *Polypterus bichir* are successful suction feeders, exhibiting the classic anterior-to-posterior wave of skull expansion. In *P. bichir*, lateral skull expansion and hyoid depression occur and are likely important for successful suction feeding (Lauder, 1980), but we do not fully understand their contributions to the volumetric expansion of the buccal cavity, their impact on prey motion, or their role in successful prey capture.

Suction feeding is powered in part or whole by the axial muscles, with variable contributions from smaller cranial muscles, which in some cases serve to redirect forces rather than generate power directly (Camp and Brainerd, 2014). This paper focuses on the ventral linkages and drivers of jaw opening in *P. bichir*, as mechanisms of cranial elevation—driven by epaxial muscles—have been elucidated previously (Lauder, 1980). In most bony fishes, as in

polypterids, the hypaxial and sternohyoideus muscles are both active during suction feeding, driving ceratohyal motion and ultimately contributing to jaw depression (Tchernavin, 1948). Hypaxial muscles insert on the cleithra, while the sternohyoideus runs between the cleithra and the anterior ceratohyals. Both muscles are active at the start of a feeding strike in *Polypterus* (Lauder, 1980) and there are three major ways that these muscles may work in concert or opposition to drive ventral expansion. First, the hypaxials may isometrically or eccentrically stabilize the cleithrum, while the sternohyoideus pulls against this “anchor” to retract and depress the ceratohyal, as proposed for bichirs, bowfin, and gar (Lauder, 1980). Second, the hypaxials may retract the cleithrum, while the sternohyoideus is isometrically active or lengthening, its activity serving to transfer force generated by the hypaxials, as demonstrated in largemouth bass and several clariid catfishes (Camp and Brainerd, 2014; Camp et al., 2015; Van Wassenbergh et al., 2005; Van Wassenbergh et al., 2007). Third, the two muscles may work in concert, both shortening to retract the cleithrum and the ceratohyal, as seen in one clariid catfish, bluegill sunfish, and striped surfperch (Camp et al., 2018; Lomax et al., 2020; Van Wassenbergh et al., 2007). The relative sizes of the sternohyoideus and hypaxial muscles are thought to determine which of these mechanisms is utilized for a given species (Lomax et al., 2020), suggesting that *P. bichir*’s extensive hypaxial muscles may drive hyoid motion indirectly through a ligament-like function of the sternohyoideus.

A deeper understanding of the mechanics of jaw opening, oral cavity volume change, and suction feeding forces in *P. bichir* and other actinopterygians requires the ability to precisely quantify motions of internal skull structures such as the hyoid arch and its connections to the cleithrum and mandible. Here, we use the X-ray Reconstruction of Moving Morphology (XROMM) workflow (Brainerd et al., 2010) and dynamic endocast modeling (Camp et al., 2015)

to quantify cranial kinesis and measure volumetric expansion of the oral cavity in *P. bichir* during feeding. We test the relationships between these motions and suction feeding forces and explore the role of the sternohyoideus and ventral hyoid arch in jaw opening in this species with three sets of analyses.

We first quantify the kinematics and relative timing of neurocranial elevation, cleithral retraction, suspensorial and opercular flaring, and jaw and hyoid depression in *P. bichir*. We hypothesized that jaw depression and neurocranial elevation precede ceratohyal depression, followed by abduction of the suspensorium and operculum, as this would maintain the anterior to posterior wave of cranial expansion thought to be common to all aquatic suction feeders.

Second, we investigated the kinematic drivers of successful suction feeding in *P. bichir* using two metrics: first by measuring motion (acceleration) of marked prey items throughout the strike and cross-correlating this motion with bone velocity; and second by employing a novel bone freezing method to measure the instantaneous contribution of each bone's motion to buccal cavity volume change. Importantly, the neurocranium was used as a frame of reference to make these measurements and therefore contributions of the neurocranium to suction generation were not measured in this study. We hypothesized that ceratohyal and jaw depression are the most important factors in successful suction generation due to their substantial and rapid motion, while lateral flaring of suspensorium and operculum influence suction generation to lesser degrees.

Finally, we evaluate the role of the sternohyoideus muscle in the linkage between the hypaxial muscles and lower jaw by measuring sternohyoideus length and translations at key points in this linkage. We hypothesized that, as in bass, the cleithrum moves posteriorly during the strike in *P. bichir*, and the sternohyoideus functions isometrically to transmit that force into

displacement of the ceratohyal, which in turn transmits force to the mandible through the mandibulohyoid ligament (MHL).

## METHODS

*Animals and care:* Three live specimens (standard lengths 23.5, 23.0, and 25.0cm) of the Nile Bichir (*Polypterus bichir lapradei* Lacepède 1803) were obtained from the aquarium industry and housed singly at the University of Chicago. Fish were fed worms or live feeder fish three times weekly. Individual fish responded best to different custom tank designs, so certain individuals were transferred to an 11.4 cm wide tank on the day of or the night before data collection but were otherwise housed in 20+ gallon aquariums. Other individuals were housed for the duration of their data collection in a “tunnel tank”, which consisted of a 24 cm by 33 cm rectangular area with a tunnel extension of 47 cm by 3.75 cm. All husbandry and experimental protocols were approved by the University of Chicago IACUC (protocol #72365).

*Surgical marker implantation:* Fish were anesthetized with 0.07- 0.3 g L<sup>-1</sup> MS-222 (added progressively, buffered 2x by weight with sodium bicarbonate) and implanted with 3-6 radio-opaque tantalum beads (1 mm or 0.8 mm) in each bone or structure of interest: neurocranium, mandible, ceratohyal, suspensorium, operculum, cleithrum, and body (Figs 1 and S1). The suspensorium (palatoquadrate + hyomandibula) was treated as a single rigid body due to firm connections between the bones (Allis, 1922) and we confirmed a lack of flexion between the two bones using pairwise inter-marker distance comparisons from 10 animated trials (within palatoquadrate =  $0.1 \pm 0.007$  mm, within hyomandibula =  $0.074 \pm 0.005$  mm, between bones =  $0.11 \pm 0.003$  mm). Body markers were implanted bilaterally approximately 6-10 cm behind the cleithrum along the most lateral points of the fish's body, with two markers just dorsal to a

frontal plane through the vertebral centra and one just ventral on each side. Body plane markers were used to animate a reference plane from which to measure neurocranial elevation and cleithral retraction (*sensu* Camp and Brainerd, 2014). Bone markers were implanted unilaterally (right side) by hand drilling and press-fitting markers into a hole of the same diameter as the marker. Soft tissue markers were injected using a hypodermic needle of a diameter slightly larger than the marker (16 gauge), and body plane markers were placed by separating two rows of scales and puncturing the skin between them using a #11-blade scalpel.

*CT scanning:* A microCT (taken post-mortem; GE Phoenix v|tome|x 240 kV/180 kV scanner, University of Chicago Paleo-CT facility) or CT scan (taken under MS-222 sedation; Vimago L Base version, EpicaScanner) of each animal was used to create 3D polygonal meshes of each bone in Amira 5.5.0 (FEI Company, Hillsboro OR), allowing precise measurement of bead placements within the bones.

*XROMM data collection and animation:* *P. bichir* were filmed feeding in custom-built tanks (described under “animal care”, designed to minimize the attenuation of x-rays through large quantities of water in the capture volume) using two pairs of roughly orthogonal X-ray sources and image intensifiers. 16 of 18 strikes used in this study were collected at the University of Chicago XROMM facility, using high-speed video cameras (Xcitex XC-2M) controlled by ProCapture motion capture software. Two additional strikes by one individual from this study were recorded at the Keck XROMM Facility at Brown University using Phantom v.10 high-speed cameras (Vision Research, Wayne, NJ, USA). All data were collected at 500 Hz using a shutter speed of 1/1000 s; the two strikes recorded at Brown did not show any kinematic differences from the 16 strikes obtained at University of Chicago.

To ensure that the feeding event occurred within the XROMM capture volume, fish were trained to strike at a minnow (*Pimephales promelas*, ~3 – 4 cm) when it was released from behind a trapdoor. Eighteen usable trials were obtained (7, 7, and 4 from each fish), two of which were failed strikes (the feeder fish was not captured). Failed strikes did not differ kinematically from successful ones, so the 18 trials were pooled together for kinematic descriptions and volumetric simulations. The two failed strikes were removed from analyses that involved prey acceleration as those prey accelerations could have been induced by the predator, by an escape response, or some other hydrodynamic effect that we could not account for. A subset of trials with a slightly higher degree of noise in rigid body transformations was removed from the volumetric analysis due to a disproportionate effect of noise on the relative contribution calculations (see “Volumetric analysis” section). This resulted in a reduced sample size of 13 strikes (7 and 6 from two fish) for the volumetric analysis.

XMALab (version 1.5.5; Knorlein et al., 2016) was used to remove image distortion, compute 3D camera positions, and track tantalum markers in each sequence. The XYZ coordinates of each marker were triangulated and used to calculate the rigid body transformation of each bone, which were exported from XMALab unfiltered. Data with obvious high-frequency noise (from the operculum and suspensorium) were later filtered using a low-pass Butterworth filter at a cutoff frequency of 50 Hz in R (version 3.5.3). Mean precision for co-osseous inter-marker distances from *in vivo* data was 0.109 mm (Table S1) (Brainerd et al., 2010).

Animations of these bone meshes were generated and motion was quantified using Maya 2018 (Autodesk, Inc., San Rafael, California) and the XROMM Maya Tools shelf version 2.2.3 ([https://bitbucket.org/xromm/xromm\\_mayatools/src/master/](https://bitbucket.org/xromm/xromm_mayatools/src/master/)). Bone mesh animations were checked against MayaCams to verify proper alignment and calibration (see Fig. 2). We used a

combination of anatomical coordinate systems (ACSs) and joint coordinate systems (JCSs) to describe various components of motion in the *P. bichir* skull during feeding strikes. An ACS refers to a 3-axis coordinate system digitally fixed to a bone, which is used to measure the translation of any object relative to that bone (Brainerd et al., 2010). Relative motion (both translation and rotation) between two bones is described using a JCS (Grood and Suntay, 1983), which in Maya consists of two ACSs – one parented to each bone of interest (Brainerd et al., 2010; Gidmark et al., 2015). Importantly, JCS rotational axes do not stay orthogonal: the Z axis is fixed to the proximal bone and the X axis is fixed to the distal bone, while the Y axis is calculated as close as possible to the normal of the other two axes (Brainerd et al., 2010). We used a global ACS to measure the motion of the prey item through world-space and calculate the Euclidean distance of prey motion. We took the first and second derivatives of this Euclidean distance to calculate the velocity and acceleration of the prey item, respectively. All values reported are peak magnitudes and timings averaged by trial ( $\pm$  standard error), while figures show values averaged by time (trials aligned to 0 ms at peak gape prior to averaging).

*Kinematic analyses:* In order to quantify the overall kinematic pattern of *P. bichir* strikes, we used JCSs oriented along anatomical directions (AP = anteroposterior, DV = dorsoventral, ML = mediolateral), thereby describing the rotations of bones in a manner comparable to that used to report data collected from lateral light camera video recordings (i.e., Grubich, 2001; Lauder, 1980; Lemberg et al., 2019; Markey et al., 2006; Sanford, 2001; Westneat and Wainwright, 1989). Each JCS was oriented such that the highest degree of motion is captured by the Z-axis to minimize non-linear distortions introduced by measuring with Tate-Bryan angles in Euler space (Manafzadeh and Gatesy, 2020). Specifically, the Z-axes for neurocranial elevation, lower jaw depression, cleithral retraction, and ceratohyal depression were all oriented mediolaterally, in

order to capture rotations in sagittal planes, while the Z-axes for suspensorial and opercular abduction were oriented anteroposteriorly, in order to capture rotations in transverse planes. Fig. 3 shows the placement of each JCS when the fish is in resting pose (solid colored bones). The neurocranium and cleithrum were measured relative to a body plane averaged across five or more body markers (after Camp and Brainerd, 2014), and the cleithrum, operculum, suspensorium, lower jaw, and ceratohyal were measured relative to the neurocranium (note that cleithral rotations were quantified in two coordinate systems to detangle the impact of neurocranial rotation and vertebral column bending from this measurement). Z-axis rotations for this overall kinematic description dataset were standardized to a starting point of 0° by subtracting the mean of the first 25 frames recorded before the strike, during a period with relatively little intracranial movement.

Initial observations and associations with volume and suction (described below) revealed substantial rotations of the ceratohyal around all three axes, so ceratohyal kinematics were further analyzed using a JCS placed in a “joint-oriented” position: with the X-axis aligned with the long axis of the bone, allowing direct measurement of ceratohyal long-axis rotation. This JCS is shown in Fig. 4A-B and was used to quantify the rotations and translations about each axis of the ceratohyal relative to the neurocranium. For this dataset, we show the untransformed (i.e., not “zeroed”) axes of rotation and translation, as these axes represent a full six degrees-of-freedom joint pose as rotations from an arbitrary resting position. Additionally, we visualized these motions using an instantaneous helical axis (Berme et al., 1990; Iriarte-Diaz et al., 2017), which completely describes bone motion as rotation about and translation along a single axis, using published MATLAB code (available at [https://github.com/jdlaurence/XROMM\\_HelicalAxis](https://github.com/jdlaurence/XROMM_HelicalAxis)). We selected the time point of peak ceratohyal velocity, or the time point at which the ceratohyal

is rotating most rapidly (-14 ms before peak gape, Fig. 6, Table 1), as a representative point for visualizing this axis of rotation during ceratohyal depression.

*Testing correlates of prey acceleration:* To estimate the contributions of each axis of cranial kinesis to prey motion, we used an ACS system paired to the neurocranium to quantify relative motions of the points on the lower jaw, ceratohyal, operculum, and suspensorium (see Fig. 6) that experienced the greatest displacements. In addition, for the ceratohyal, we selected both anterior and posterior points, as this bone undergoes substantially different motions at each end. We calculated the velocity (derivative of the Euclidean distance traveled) for each of these points relative to the neurocranium. We then used cross-correlation analyses to determine the temporal relationships between velocity of motion at each key point and prey acceleration, a proxy for suction force. We compare the velocity of bones and acceleration of prey because the acceleration of water around a prey item is thought to determine the force applied to that prey, and is driven by the rate of cranial expansion (Holzman et al., 2008; Wainwright and Day, 2007). Analyses of bone velocity to prey velocity provided similar results and are therefore not included in the present study. Cross-correlations calculate the linear correlation between two time series across a set of lags, where, for each lag, one signal is shifted in time relative to the other. We calculated maximum (positive) cross-correlations from 50 ms before and after peak gape (100 ms total) using a modified version of the R function `ccfDis` (matools package, <https://aaronolsen.github.io/software/matools.html>), which adds “NA” buffers corresponding to the lag time between each concatenated time series to prevent overlap of signals from different trials when time series are shifted. We tested significance for each motion pair after Olsen et al. (2019), where we randomly inverted one signal for each trial generating a null distribution of 999 unique iterations for all bones except the suspensorium (this bone was properly animated in a

lower number of trials and thus could only have 256 unique randomized iterations). Due to the concatenation of time series from all trials required for this statistical test, we do not present  $\pm$  standard error of R values for this cross-correlation dataset.

*Volumetric analysis:* We expanded our testing of the contributions of the operculum, suspensorium, ceratohyal, and jaw to suction generation using volumetric analysis and virtual iterative bone freezing experiments. The instantaneous volume of the oral cavity was measured by creating a dynamic digital endocast of the right side of the head, and reported volume measurements are doubled to reflect total mouth volume (*sensu* Camp et al., 2015). In Maya, locators were attached to the oral surfaces of the animated cranial bones, and their locations over time were calculated. The locator positions were then imported into MATLAB (R2020a), where, for every frame, an alpha shape was calculated from the constellation of locators, and its volume was computed using code adapted from (Camp et al., 2015) (Fig. S2A-B). Adapted code may be accessed at: <https://github.com/jdlaurence/dynamicEndocastByBone>.

In order to measure the instantaneous contributions of the lower jaw, ceratohyal, suspensorium, and operculum to the overall change in oral cavity volume, we developed a new method of digitally freezing bones to the neurocranium. We chose not to measure the RCVC of the cleithrum, as there is not clear evidence that cleithral retraction will directly change the shape of the posterior oral cavity. Traditionally, freezing a degree of freedom in a biomechanical system to assess its impact on a motion involves holding that degree of freedom frozen for the duration of the motion (Bernstein, 1967; Olsen, 2019; Vereijken et al., 1992). However, given the extreme range of motion in bones like the ceratohyal and lower jaw and potential for inter-bone interaction effects at different points in a strike, we progressively froze the given bone relative to the neurocranium for short time increments (5 frames, 10 ms), on a rolling basis over

the duration of a trial. This allows an instantaneous quantification of the effect of a given bone's motion on volume change throughout the strike, rather than averaged across total strike duration. We selected five frames as our preferred freezing interval as this was a short enough period to avoid creating any joint poses that could not easily be achieved by cadaveric manipulations or observed during *in vivo* data collection, which we confirmed by importing alpha hulls back into Maya for visualization (see Fig. S2B-J). Additionally, we examined the Delta Volume Full traces (difference of total endocast volume between consecutive increments) with different increment values and noted that the peak at maximum expansion rate began to widen at increments above 10-15 ms, suggesting over-smoothing.

The individual skeletal element freezing was performed by the MATLAB function 'dynamicEndocastByBone', which calculates the transformation matrix describing the motion of the reference bone (neurocranium) from one time step,  $t$ , to the next,  $t+I$  (where  $I$  is one increment of five frames), and then applying that transformation matrix to the bone to be frozen. So, at every  $t+I$  frame, five alpha shapes were calculated: the alpha shape from baseline animation with all bones moving and four alpha shapes with a single bone (lower jaw, ceratohyal, suspensorium, or operculum) 'frozen' in its position relative to the neurocranium at frame  $t$ . Consequently, the difference in any frame  $t+I$  between the frozen volume and the baseline volume represents the impact of that frozen bone on the overall volume change at that time.

To quantify the relative contributions of each bone and normalize this to the change in volume at a given time point, we took the difference between the overall volume change and the frozen volume change for each bone and divided it by the sum of absolute volume changes for

all frozen bones. Thus, the instantaneous relative contribution to volume change (RCVC) of the  $i$ th bone ( $RCVC_{Bone_i}$ ) is represented by the following equation:

$$RCVC_{Bone_i} = \frac{\Delta V_{Full} - \Delta V_{FrozenBone_i}}{\sum_{j=1}^n |\Delta V_{Full} - \Delta V_{FrozenBone_j}|}$$

Where for a given time increment:  $\Delta V_{Full}$  is the change in endocast volume without any bones frozen,  $\Delta V_{FrozenBone_{i/j}}$  is the change in endocast volume with the  $i$ th or  $j$ th bone frozen, and  $n$  is the number of bones frozen (i.e., does not include the neurocranium). A bone's RCVC is a unitless ratio of its impact on endocast volume change to the sum of all bones' impacts on volume change at a given time point. We use the sum of impacts of all frozen bones in the denominator rather than the total volume change to avoid singularities and magnified noise effects associated with the small denominators that occur when the net volume change approached zero but individual bones were still moving. Thus, RCVC constitutes a stable measure of the impact of a given bone's motion on the volume change of the buccal cavity relative to the cumulative impact (in absolute terms) of all bones. Importantly, the absolute value signs in the denominator of the equation remove the directionality of volume change; only when all bones are contributing to expansion (RCVC is positive for all bones) or all are contributing to compression (RCVC is negative for all bones), can RCVC be interpreted as the relative contribution to overall oral volume expansion or contraction, respectively. For example, if a bone's RCVC is positive, then that bone is contributing to oral cavity volume expansion, but the oral cavity could be experiencing either net expansion or contraction at that time.

All volumetric data were smoothed using a three-frame moving average filter. Trials in this analysis were cut off at -35 to 50 ms before extracting bone contribution peak magnitudes and times because high amounts of noise prior to the onset of bone motion led to false peaks in

some values. We tested for significant differences between bone's RCVCs at several time points among all ( $n = 13$ ) *P. bichir* strikes pooled using a one-way ANOVA and post-hoc Tukey HSD tests. For this analysis, we selected the time at each bone's peak RCVC, time at peak total volume, and time at peak rate of volume change as our time points of interest.

*Examining evidence for a cleithrum-hyoid-jaw linkage:* To evaluate the role of pectoral girdle displacement and sternohyoideus function on ceratohyal and lower jaw kinematics, translation of the cleithrum and ceratohyal were measured relative to the neurocranium using ACSs. Specifically, we quantified the displacement magnitudes of the most ventrolateral aspect of the cleithrum (lateral sternohyoideus origin), the most anterior aspect of ceratohyal (sternohyoideus insertion), most posterior aspect of ceratohyal (mandibulohyoid ligament origin), ventral lower jaw just anterior to the palatoquadrate joint (mandibulohyoid ligament insertion), and most anterior aspect of the lower jaw (to measure jaw depression) (see Fig. 7). We quantified these motions in all three anatomical planes, measuring protraction-retraction (anterioposterior translation), elevation-depression (dorsoventral translation), and adduction-abduction (mediolateral translation). The relationship between retraction of the cleithrum, depression and retraction of the ceratohyal, and depression and retraction of the lower jaw were analyzed pairwise across bones using cross-correlations. Cross-correlation provides a measure of association between two time series variables across a series of lags (see above), so we use them here to investigate potential cause-effect relationships among kinematics of different overall excursion magnitude. We report the highest (absolute value) cross-correlations from 50 ms before and after peak gape (100 ms total) across trials and the lag time at which the maximal cross-correlation occurred. Variables with consistent (low deviation) lag times and high R values are identified as motions likely to be causally linked (e.g., driven by the same musculature or

motion of one bone actuating motion of another in a linkage). A distance tool was used to measure the length of the sternohyoideus muscle, approximated with locators at the insertion and origin sites of the muscle (both lateral and medial origins) (see Fig. 7).

## RESULTS

Suction feeding in *Polypterus bichir* involves a highly kinetic skull, with elevation of the neurocranium and depression of the lower jaw initiating a rapid increase in gape to begin the strike, followed by cleithral retraction and ceratohyal depression, and finally by lateral abduction of the operculum and suspensorium. *P. bichir* employ forward-directed ram feeding in addition to suction, and a wave of dorsoventral bending travels posteriorly down the body (Fig. 2). Prey acceleration peaks rapidly and the prey maintains relatively constant velocity through the expansive phase of the strike, slowing once it reaches the back of the pharynx. Prey acceleration was most strongly cross-correlated with lower jaw and anterior ceratohyal velocity. The ceratohyal undergoes complex 3D motions, depressing, retracting, flaring laterally and rotating about its long axis. Changes in oral cavity volume were driven initially by the lower jaw, then the ceratohyal, and finally by the operculum. The sternohyoideus muscle does not shorten during strikes and this study supports force transmission between the ceratohyal and lower jaw through the MHL.

### *Kinematic pattern of Polypterus bichir feeding strikes*

*P. bichir* feeding strikes start with a rapid gape increase, driven by neurocranial elevation (maximum  $33.6 \pm 4.67^\circ$  SEM relative to the body plane) and lower jaw depression (maximum  $-34 \pm 0.79^\circ$  relative to the neurocranium) (Fig. 2, Fig. 3, Table S2). Shortly after the onset of cranial elevation and jaw depression, the ceratohyal begins depressing (maximum  $-55.3 \pm 1.55^\circ$ ), reaching its peak  $14 \pm 3.01$  ms after maximum gape. Posterior rotation of the cleithrum relative to the neurocranium (maximum  $-32.4 \pm 0.97^\circ$ ) follows a pattern similar to the ceratohyal, peaking slightly earlier at  $10.7 \pm 3.0$  ms after peak gape. Posterior rotation of the cleithrum relative to the body plane reached a minimum of  $7.6 \pm 1.21^\circ$  at  $-24.5 \pm 2.24$  ms and a maximum of  $-31.5 \pm 3.11^\circ$  at  $37.6 \pm 3.77$  ms. Finally, the operculum and suspensorium abduct, reaching their peaks of  $19.1 \pm 1.0^\circ$  and  $12.8 \pm 1.1^\circ$  at  $24.6 \pm 2.17$  ms and  $30.9 \pm 6.6$  ms after peak gape, respectively (Fig. 3, Table S2). Opercular adduction (average peak of  $-3.7 \pm 0.61^\circ$  across trials) also occurs at the onset of the strike, at  $-15.9 \pm 6.48$  ms before peak gape (Fig. 3).

The ceratohyal of *P. bichir* exhibited substantial rotation about each axis, in addition to the anatomically-oriented z-axis (depression) described above. Noting substantial long-axis rotation of the ceratohyal in our animations, we quantified the motion of this bone using an additional set of JCSs, oriented such that the x-axis directly measured long-axis rotation of the bone (Fig. 4). Translation and rotation data in this “joint-oriented” JCS measured relative to the neurocranium (Fig. 4) demonstrate that the ceratohyal rotates  $-80.0 \pm 2.89^\circ$  about its long axis,  $60.1 \pm 1.5^\circ$  about a mediolaterally oriented z-axis, and  $-28.1 \pm 1.98^\circ$  around a primarily dorsoventral axis. Additionally, the ceratohyal translates in all 3 of these directions, with particularly high lateral ( $-14.5 \pm 0.71$  mm) and posterior ( $-6.03 \pm 0.32$  mm) translations. We also visualized ceratohyal movement using an instantaneous helical axis, which describes rigid

motion as a rotation and a translation along a single axis, shown in Fig. 4E-F. At peak ceratohyal velocity, the axis of rotation of the ceratohyal is at approximately 45° to both the mid-sagittal and frontal planes. This axis is dorsal and anterior to the joint of the ceratohyal with the interhyal when measured relative to the neurocranium (Fig. 4E-F).

### *Drivers of oral cavity volume change*

Volumetric analysis shows that oral cavity volume began increasing at  $-28.8 \pm 1.61$  ms across all measured trials, peaking to  $13.5 \pm 0.9$  cm<sup>3</sup> at  $11.5 \pm 1.88$  ms. The absolute rate of volume change peaked at  $-10.9 \pm 1.00$  ms (Table 2, Fig. 5). Across trials, the relative contribution to volume change (RCVC) of the lower jaw reached the highest peak of  $0.77 \pm 0.03$  first in the strike at  $-26.3 \pm 1.34$  ms and was significantly different from all other bones at this time ( $p < 0.0001$ ). The ceratohyal RCVC peaked later in the strike and contributed slightly less to instantaneous volume change, reaching a peak of  $0.61 \pm 0.04$  at  $-4.6 \pm 3.17$  ms, also significantly higher than all other bones at this time ( $p < 0.0001$ ). The suspensorium reached the lowest peak RCVC of  $0.48 \pm 0.09$  shortly after peak gape at  $5.4 \pm 1.84$  ms (Table 2) and was statistically different from the ceratohyal and lower jaw ( $p < 0.01$ ), but not the operculum ( $p = 0.561$ ) at this time. Finally, the operculum RCVC reached the latest peak of  $0.63 \pm 0.06$  at  $10.0 \pm 3.50$  ms and was significantly different from all other bone's RCVC at this time ( $p < 0.01$ ). When considering each bone's peak RCVC regardless of time point, significant differences were found only between the lower jaw and the suspensorium ( $p < 0.01$ ).

At the point of maximum rate of volume change, the ceratohyal's RCVC was significantly higher than all other bones ( $p < 0.0001$ ), followed by the lower jaw and operculum (which were not statistically different,  $p = 0.91$ ), and finally the suspensorium (Table 2). At maximum total volume, the operculum's RCVC was highest and significantly different from the lower jaw and ceratohyal ( $p < 0.01$ ), but not from the suspensorium ( $p = 0.23$ ). Analysis of the RCVC of each bone averaged by time point shows that the lower jaw contributes most strongly to volume changes from the onset of the strike until 14 ms before peak gape (Fig. 5). Between -14 ms and peak gape, the contributions of the ceratohyal rapidly overtake those of the lower jaw (Fig. 5). Just prior to peak gape (-4 ms) the operculum RCVC overtakes the ceratohyal contributions, and the operculum contributes most substantially to volume change at the end of the strike. Suspensorial RCVC also peaks later in the strike, overtaking ceratohyal contributions at 2 ms, but never reaches a higher RCVC than the operculum (Fig. 5).

#### *Correlates of prey acceleration*

Cross-correlation analyses demonstrated that displacement velocities for all bones except the suspensorium were significantly associated with prey acceleration ( $p < 0.05$ , determined by null distributions with  $> 999$  unique combinations for all bones except suspensorium). Statistical power for the suspensorium was lower than for other bones due to a reduced total number of successful trials in which this rigid body was effectively reconstructed (9 trials, null distribution included 256 unique combinations). Displacement velocity of the anterior lower jaw correlated most strongly with prey acceleration ( $R = 0.302$ ) and had the lowest lag time at 1 ms (Fig. 6, Table 1). Anterior ceratohyal velocity followed shortly behind in both lag (3 ms) and maximum correlation ( $R = 0.296$ ) (Fig. 6, Table 1). We did not test the relationship between cleithral

velocity and prey acceleration, as cleithral motion should indirectly contribute to suction generation through linkages with cranial elements measured in this study. The operculum had a relatively lower correlation with prey acceleration ( $R = 0.219$ ) and a higher lag time at 10 ms (Fig. 6, Table 1). Finally, the suspensorium had the lowest cross-correlation ( $R = 0.1$ ) and the highest lag time (17 ms).

### *Cleithrum and jaw opening linkage mechanics*

The insertion of the lateral sternohyoideus on the ventrolateral aspect of the cleithrum (Fig. 6) retracts to a maximum of  $-18.4 \pm 1.18$  mm relative to the neurocranium at  $14.7 \pm 3.70$  ms (averaged across trials) (Table S3). At the onset of cleithral motion, this point elevates slightly ( $2.1 \pm 0.39$  mm at  $-31.8 \pm 2.14$  ms), then depresses over an extended period, to a negative peak of  $-8.5 \pm 0.43$  mm at  $36.7 \pm 2.43$  ms (Table S3). The anterior ceratohyal, which is connected directly to the measured cleithral point by the sternohyoideus, retracts to a maximum of  $-20.5 \pm 1.02$  mm at  $11.7 \pm 1.91$  ms and depresses to a negative peak of  $-20.7 \pm 0.57$  mm at  $15.7 \pm 3.03$  ms (Table S3). The posterior ceratohyal retracts much less (a peak of  $-5.5 \pm 0.39$  mm at  $-11.3 \pm 1.42$  ms) and elevates to a maximum of  $3.9 \pm 0.34$  mm at  $20.0 \pm 3.28$  ms. The largest translation of the posterior ceratohyal is lateral, to a peak of  $16.3 \pm 0.7$  mm at  $9.2 \pm 1.73$  ms (Table S3). Distance measurements between the lateral-most and medial-most origins to a single insertion point of the sternohyoideus demonstrate that this muscle is not shortening during strikes; in fact, the muscle lengthens during the compressive phase (Fig. 7C).

The mandibulohyoid ligament (MHL) attachment on the lower jaw translates anteroposteriorly and dorsoventrally in phase with the posterior ceratohyal, reaching a posterior maximum of  $-3.5 \pm 0.23$  mm at  $-9 \pm 1.48$  ms, and ranging from a dorsal maximum of  $3.2 \pm 0.27$  mm to ventral maximum of  $-2 \pm 0.27$  mm (Table S3). The MHL attachment point on the lower jaw translates laterally to a peak of  $7.3 \pm 0.43$  mm (Table S3). Fig. 7 shows these motions averaged by time point across trials.

Cross-correlations demonstrate a strong relationship and minimal lag ( $1 \pm 0.04$  ms and  $0.22 \pm 0.22$  ms, respectively) between the posterior translation of the lateral aspect of the cleithrum and the posterior and ventral translations of the anterior ceratohyal ( $R = 0.953 \pm 0.011$  and  $0.944 \pm 0.008$ , respectively). There is also a strong correlation between ceratohyal motion and lower jaw depression, with ventral translation of the anterior lower jaw (jaw depression) strongly correlated with both posterior motion across the ceratohyal ( $R = 0.863 \pm 0.015$  and  $0.867 \pm 0.015$ ,  $5.1 \pm 0.69$  and  $-2.67 \pm 0.4$  ms lag) (anterior and posterior ceratohyal, respectively) and dorsoventral translation of the anterior ceratohyal ( $R = 0.773 \pm 0.019$ ,  $5.78 \pm 0.62$  ms lag) (Fig. 7, Table 3). The lower jaw at the MHL attachment site shows relatively little motion (Fig. 7) and largely lower cross-correlations or more variable lag times with motion at the posterior ceratohyal. The clearest relationships are between posterior ceratohyal retraction and retraction of the lower jaw at the MHL ( $R = 0.91 \pm 0.014$  at 0 ms lag across all trials) and elevation of the posterior ceratohyal and elevation of the lower jaw at the MHL ( $R = 0.774 \pm 0.033$  at  $-7.11 \pm 2.11$  ms). (Table 3). Posterior translation of the cleithrum and ventral translation of the anterior lower jaw ( $R = 0.801 \pm 0.024$  with a  $7.67 \pm 1.26$  ms lag) are also highly correlated.

## DISCUSSION

The kinematics of the cranial bones of *P. bichir* during feeding strikes enable us to test hypotheses about the mechanisms driving the suction which underlies successful prey capture. In *P. bichir*, jaw opening initiates suction generation via rapid volumetric expansion of the oral cavity, while ceratohyal depression enhances and maintains suction and oral cavity expansion. Opercular abduction also contributes substantially to volume increase in the oral cavity, but its timing later in the strike serves not to generate suction directly but to maintain successful prey capture by allowing water to exit through the gills, maintaining the momentum of the water bolus throughout the strike. We also present new evidence for a previously proposed biomechanical linkage between the cleithrum, ceratohyal, and lower jaw. This linkage utilizes cleithral retraction to transfer power generated by the hypaxial muscles through an isometrical sternohyoideus muscle to the anteroventral hyoid arch, driving not only ceratohyal depression but also retraction and long-axis rotation, ultimately enabling jaw opening.

### *Kinematic patterns of Polypterus bichir feeding strikes*

Suction feeding in *P. bichir* involves an anterior to posterior wave of motion in the body, cranium, lower jaw, and hyoid apparatus (Figs. 2 & 3), the same sequence utilized by teleosts and other aquatic suction feeders (Bishop et al., 2008; Jacobs and Holzman, 2018). This confirms previous work (Lauder, 1980) while expanding our knowledge of motion in bones such as the ceratohyal, cleithrum, and suspensorium, which are partially or wholly obscured and therefore unmeasurable by light camera video (Figs. 3 & 4). We additionally note substantial, previously undescribed, dorsoventral flexion in the vertebral column during *P. bichir* strikes, and posit that

these fish appear to utilize numerous intervertebral joints to accommodate a large degree of neurocranial elevation as recently described in both trout and frogfish (Camp, 2021).

Contrary to a previous hypothesis that the pectoral girdle of *Polypterus* serves as a stable anchor point for sternohyoideus muscle activity (Lauder, 1980), this study demonstrates that the cleithrum in *P. bichir* is highly mobile, undergoing substantial retraction during suction feeding strikes (Fig. 3). Interestingly, cleithral retraction relative to the neurocranium breaks the “anterior to posterior” pattern, as it peaks well before suspensorial or opercular abduction, although this pattern of mobility still holds within the skull. We demonstrate that cleithral mobility contributes to hyoid and lower jaw motion, though the power generated by the muscles that move it (hypaxial and sternohyoideus muscles) *a la* Camp and Brainerd (2014) remains to be quantified in this species.

Historically, hyoid bar motion in fishes was measurable only when the anteroventral hyoid apparatus depressed below the level of the jaws: XROMM enables measurement of the hyoid arch throughout a strike, allowing us to quantify the rotations and translations of the ceratohyal in all three anatomical axes (Fig. 4). We found not only the substantial depression and retraction of the ceratohyal previously described in fishes (Lemberg et al., 2019; Olsen et al., 2019), but also long-axis rotation, a previously unreported motion, which may be common across actinopterygians.

#### *Drivers of suction in Polypterus bichir feeding strikes*

Jaw opening, ceratohyal depression and retraction, and lateral abduction of the operculum relative to the neurocranium are all substantial contributors to suction generation in *P. bichir*,

with oral cavity volume change being primarily driven by these three bones in sequence (Fig. 5). Each of these bone velocities was significantly cross-correlated with prey acceleration, our proxy for suction. Neurocranial elevation also contributes to volume change and prey motion, but its contributions could not be directly measured in this portion of the study because the cranium served as a reference point. While prey acceleration alone underestimates the forces acting on the water (Holzman et al., 2008), motion of the prey item into the mouth to achieve prey capture is the ultimate goal of a suction feeding event and is therefore a useful measure of suction performance. The strongest correlations and shortest lag times were between prey acceleration and jaw velocity, followed closely by ceratohyal velocity (Fig. 6, Table 1). Furthermore, the highest overall RCVCs were produced by the lower jaw at the beginning of the strike, and the ceratohyal contributed the highest RCVC at the time of highest volume change (Fig 5., Table 2). This implies that, of the kinematics measured here, an increase in gape of the oral jaws anteriorly and depression of the ceratohyal posteriorly are the two primary sources of oral cavity volume expansion during suction feeding in *P. bichir*. Additionally, increases in prey acceleration and velocity begin during a period of the strike when only the neurocranium and lower jaw have moved substantially, suggesting that *P. bichir* strikes are initiated via flat-plate suction associated with jaw opening, and subsequent ceratohyal motion serves to maintain the velocity of the prey item. While this idea has been explored in previous work (Bishop et al., 2008; Jacobs and Holzman, 2018; Lemberg et al., 2019) the ability to quantify the association between 3D motion of individual skeletal elements and a prey item tracked throughout a feeding event allows a direct test of this hypothesis.

Lateral flaring of the suspensorium and operculum are also important to successful suction feeding in *P. bichir*, but not because it initiates negative pressure in the buccal cavity. Instead, lateral flaring continues the anterior to posterior wave of oral cavity expansion, maintaining the momentum of water through the mouth by allowing it to exit through the opercular opening. This is suggested in our study by the significant cross-correlation between opercular velocity and prey acceleration (at 16 ms) (Table 1) and by the high RCVC of opercular motion, which was significantly different from all other bones at its peak (Fig. 5, Table 2) of 10 ms, following prey ingestion into the oral cavity (coincident with a decrease in prey velocity, Fig. 6). Consideration of opercular kinematics (Fig. 3) and RCVC (Fig. 5) demonstrate that the operculum is contributing to an increase in volume at this time, as it is still abducting away from the neurocranium. Interestingly, the operculum may also play a role at the start of the strike by adducting slightly (Fig. 3), similar to the volume decrease seen in the “preparatory phase” before cranial expansion, noted in some teleosts (Lauder, 1980). The function of this opercular adduction is probably to ensure that suction generated by oral cavity expansion is directed forwards, not through the gill slits. Our interpretation of the role of the suspensorium is complicated by our inability to test statistical significance at the same level of confidence as other bones, but results from cross-correlation with prey acceleration and volumetric analyses support the notion that abduction of the suspensorium is a relatively minor contributor to suction generation. However, movement of the palate relative to the neurocranium and the relative mobility of the interhyal between suspensorium and ceratohyal provides an additional degree of freedom to ceratohyal motion, perhaps enabling the complex 3D motion in the ceratohyal discussed above (Fig. 4). As proposed previously (Lauder, 1980), the flexibility afforded by the interhyal joint likely allows for an increased moment arm of the mandibulohyoid ligament

relative to the lower jaw by enhancing the degree of posterior translation possible in the ceratohyal (Figs. 4 & 7).

Many previous studies have modeled hydrodynamics of fish suction feeding using geometric shapes like cones, with varying success and assumptions required (Bishop et al., 2008; Michel et al., 2015; Muller and Osse, 1984; Muller et al., 1982; Van Wassenbergh and Aerts, 2009). The use of 3D data collection and visualization techniques, such as CT scanning and the XROMM workflow, can be paired with hydrodynamic models to elucidate the role of each functional component of the fish skull during suction feeding. While such a combined model is outside the scope of the current study, the volume-based approach and prey acceleration measurements presented here lay the foundation for future modeling work in *P. bichir*, a species with important implications for our understanding of the evolution of suction feeding mechanics across fishes.

#### *Cleithrum, hyoid, and jaw opening linkage mechanics*

Our ability to measure ceratohyal kinematics in 3D allowed not only quantification of its contribution to oral cavity volume change but also its role in transmitting forces from the cleithrum to the lower jaw to drive jaw depression. Our data show that the cleithrum is retracted and rotated posteriorly during suction strikes (Fig. 3, Fig. 7), motion that must be generated by hypaxial muscle contraction (Allis, 1922). This posterior cleithral motion is then translated into ceratohyal retraction and depression, which in turn causes mandibular depression by applying a posteriorly and dorsally directed force to the posterior mandible, behind the axis of rotation (Fig. 7, Lauder, 1980). Retraction of the cleithrum begins while the posterior ceratohyal moves

posteriorly and the anterior ceratohyal moves ventrally and posteriorly. The posterior ceratohyal stops moving posteriorly about 11 ms prior to peak gape (Fig. 7D), followed by a slight dorsal translation and an increase in its rate of lateral translation (Fig. 7E-F). We propose that this “hard stop” on ceratohyal retraction occurs when the articulation of the ceratohyal with the interhyal and suspensorium has reached its limit; continued transmission of force to the cleithrum results in anterior depression and posterior “lateral flaring” of the ceratohyal. Lateral flaring of the ceratohyal may be the primary driver of abduction in the suspensorium, which begins to increase at this time (Fig. 3) (Video S1).

We conclude that the sternohyoideus muscle is contributing little, if any, power to drive hyoid motion, despite being active during strikes (Lauder, 1980). The sternohyoideus remains the same length during the expansive phase of feeding strikes in *P. bichir* (Fig. 7) so is incapable of contributing work to ceratohyal movements. This means that, as in bass, the axial muscles are the primary driver of ceratohyal motion in the expansive phase of the suction strike in *P. bichir* (Camp and Brainerd, 2014).

Data presented here support the theory that retraction of the ceratohyal drives jaw opening in *P. bichir*. Lauder (1980) hypothesized that jaw opening torques act on the jaw through the MHL, the connection of the lower jaw to the posterior ceratohyal. This ligament inserts on the ventral surface of the jaw and is positioned behind its axis of rotation (Fig. 7B), meaning that posterior and dorsal forces applied through the MHL will result in jaw depression (Lauder, 1980). Our data demonstrate that this MHL insertion point undergoes a measurable but small degree of motion during feeding (Fig. 7). The motion at this MHL insertion point which has the clearest implications for jaw opening, retraction, peaks at -9 ms, before maximal jaw depression (Fig. 7, Table S3) and is strongly cross-correlated with retraction of the ceratohyal

(Table 3). Furthermore, although the jaw has not reached peak depression when the MHL insertion stops moving posteriorly (-9 ms), the jaw's peak velocity occurs before this point in the strike (-16 ms, Fig. 6), indicating that forces applied to the jaw at the MHL due to ceratohyal motions may be solely responsible for imparting the forces required for jaw opening.

There are two additional mechanisms that may contribute to jaw opening but were not directly measured in this study. First, while *P. bichir* lacks the levator operculi muscle thought to drive jaw depression via opercular rotation in *Amia* and teleosts (Allis, 1922; Camp and Brainerd, 2015; Lauder, 1980), we cannot rule out contributions from other muscles such as the adductor operculi or adductor hyomandibulae. It is plausible that the early opercular and suspensorial motions seen between -30 and -20ms (Fig. 3) are contributing to jaw depression early in the strike. Second, it is possible that once the jaw is opened far enough, the continued ventral movement of the anterior ceratohyal could affect additional jaw opening by applying force to the anterior lower jaw via some combination of the branchiomandibularis, interhyoideus (geniohyoideus superior in Allis, 1922), or intermandibularis posterior (geniohyoideus inferior in Allis, 1922) muscles. Regardless of the precise mechanism and origins of force transferred between the ceratohyal and the lower jaw, this study showed a clear relationship between ceratohyal motion and lower jaw depression (Table 3, Fig. 7), and further analysis is needed to understand the degree to which other mechanisms may mediate jaw opening.

Cleithral retraction also had a strong relationship with jaw opening, though with a lower R-value and more variable lags than seen for the cleithrum-ceratohyal or ceratohyal-jaw relationship (Fig. 7, Table 3). These slightly lower correlations and varied lag times are likely due to the more complex nature of this linkage, with the cleithral motion input (via sternohyoideus muscle) driving complex three-dimensional ceratohyal motions (Figs. 4 and 7) in

addition to the retraction likely causing jaw depression. Additionally, hyoid constrictor muscles may play a role in modulating the degree to which the ceratohyal depresses in response to a posteroventral force applied to its anterior aspect through the sternohyoideus, as seen in alligator gar (Lemberg et al., 2019). Future work modeling the expected linkage relationships compared to observed motions in this dataset will be of value for understanding the degree to which various muscular inputs are driving skeletal motions throughout the strike.

### *Implications for actinopterygian feeding evolution*

Polypterids are commonly used as an analog for tetrapodomorph fishes (Lemberg et al., 2021; Markey, 2006; Markey and Marshall, 2007), as these fish are considered to be the extant sister taxa to all other living actinopterygians (Coates, 2017; Giles et al., 2017). While polypterid fishes have undergone a substantial independent evolutionary history and some notable reversals (Giles et al., 2017), the presence of broader functional characteristics, including linkages in the feeding apparatus, in both *P. bichir* and extant teleosts or other actinopterygian fish leaves the most parsimonious explanation that these characters are retained throughout the early actinopterygian lineage. For example, this study confirms that *P. bichir* has a highly mobile ceratohyal and cleithrum, both of which are also present in gars and derived teleosts (Camp and Brainerd, 2014; Camp et al., 2020; Lemberg et al., 2019).

A mobile cleithrum enables contracting hypaxial muscles and an active sternohyoideus to work in concert, directly driving complex ceratohyal motions which enable jaw opening and successful feeding via suction. Similar mechanisms recently described in largemouth bass (Camp and Brainerd, 2014), bluegill (Camp et al., 2018), catfish (Camp et al., 2020), and now *P. bichir*

emphasize that the importance of hypaxial muscle contraction for feeding is likely ubiquitous in suction feeding fishes (Tchernavin, 1948), though additional power contributions from the sternohyoideus are more variable (Lomax et al., 2020; Van Wassenbergh et al., 2007). Indeed, we know that this linkage is maintained even in highly derived teleosts, all of which share a second jaw opening mechanism wherein the operculum contributes to jaw opening (Camp and Brainerd, 2015; Olsen et al., 2017). Future work modeling the ability of each of these jaw opening linkages to cause mandibular depression in species that utilize both mechanisms could be useful in understanding the evolutionary maintenance of the pectoral girdle-hyoid-jaw linkage.

A deeper understanding of *P. bichir* suction feeding also helps us to examine the basic morphological and biomechanical building blocks of successful suction feeding in fishes and even aquatic-feeding vertebrates more broadly. *P. bichir* skulls are more mobile than those of lungfish or amphibians due to the capacity for lateral expansion of the suspensorium, but they lack the mobile maxilla or premaxilla common to teleosts and *Amia*. Here we demonstrate that *P. bichir* are effective suction feeders without a high degree of maxillary mobility, utilizing volumetric expansion generated primarily by oral jaw and ceratohyal motion (relative to the neurocranium) to pull prey items into their mouth (Figs. 5 & 6). We show that the impact of a mobile suspensorium on volumetric change in the oral cavity is relatively small. It is possible that this mobility is just as important for allowing the full range of motion seen in the ceratohyal (ie. Fig. 4 & 7) as it is for its direct role in contributing to suction generation or oral cavity volume change. The role of a mobile suspensorium could be more rigorously tested by examining other species with an immobile suspensorium using modeling and volume experiments similar to those presented here.

## Conclusion

We demonstrate that jaw opening generates the suction forces that initiate prey motion during *P. bichir* feeding strikes. Complex ceratohyal motion enhances and maintains volumetric expansion to drive successful suction feeding in this species. Continued application of the volume modeling techniques developed in this study to other taxa will help elucidate the basic building blocks of suction feeding across actinopterygians. Kinematic evidence presented here supports a central role of the ceratohyal in mediating the biomechanical linkage between the cleithrum and lower jaw and suggests that motion in this linkage is powered by the axial muscles. Future modeling using these data could inform precisely how force is transmitted from the ceratohyal to produce jaw depression in actinopterygian fishes both without and in concert with an opercular jaw opening linkage.

## ACKNOWLEDGEMENTS

We thank Samantha Gartner, Kelsey Stilson, Elska Kaczmarek, and Michael Coates for surgical assistance, technical help, and thoughtful discussions. Three constructive reviews greatly improved the manuscript. We thank Sofia Garrick for assistance with data processing and Dave Baier for MayaTools. Thanks to the University of Chicago XROMM Facility, Brown University Keck Lab, University of Chicago Paleo-CT, University of Chicago Veterinary CT, University of Chicago Animal Resources Center, and University of Chicago Research Computing Center for facilities use and resources. This is University of Chicago XROMM Facility Publication #10.

## COMPETING INTERESTS

The authors declare no competing or financial interests.

## FUNDING

This work was funded in part by the University of Chicago Henry Hind's Fund and University of Chicago Integrative Biology Core Facilities Fund. Funding for the UChicago XROMM Facility was provided by National Science Foundation Major Research Instrumentation Grants MRI 1338036 and 1626552.

## DATA AVAILABILITY

Raw videos, tracked trials, and bone meshes used in this manuscript are accessible on the XMA portal under identifier portal\_base5 and can be accessed here:

[https://xromm.rcc.uchicago.edu/larequest.php?request=explorePublicMetadataStudy&StudyID=5&instit=portal\\_base](https://xromm.rcc.uchicago.edu/larequest.php?request=explorePublicMetadataStudy&StudyID=5&instit=portal_base).

## REFERENCES

- Alexander, R. M. N.** (1967). The functions and mechanisms of the protrusible upper jaws of some acanthopterygian fish. *J. Zool.* **151**, 43–64.
- Allis, E. P.** (1922). The Cranial Anatomy of Polypterus, with Special Reference to Polypterus bichir. *J. Anat.* **56**, 189-294.43.
- Berne, N., Cappozzo, A. and Meglan, J.** (1990). Rigid body mechanics as applied to human movement studies. *Biomech. Hum. Mov. Appl. Rehabil. Sport. Ergon.* 89–102.
- Bernstein, N.** (1967). *The co-ordination and regulation of movements*.

- Bishop, K. L., Wainwright, P. C. and Holzman, R.** (2008). Anterior-to-posterior wave of buccal expansion in suction feeding fishes is critical for optimizing fluid flow velocity profile. *J. R. Soc. Interface* **5**, 1309–1316.
- Brainerd, E. L., Baier, D. B., Gatesy, S. M., Hedrick, T. L., Metzger, K. A., Gilbert, S. L. and Crisco, J. J.** (2010). X-ray reconstruction of moving morphology (XROMM): precision, accuracy and applications in comparative biomechanics research. *J. Exp. Zool.* **313A**, 262–279.
- Camp, A. L.** (2021). A neck-like vertebral motion in fish. *Proc. R. Soc. B Biol. Sci.* **288**,.
- Camp, A. L. and Brainerd, E. L.** (2014). Role of axial muscles in powering mouth expansion during suction feeding in largemouth bass (*Micropterus salmoides*). *J. Exp. Biol.* **217**, 1333–1345.
- Camp, A. L. and Brainerd, E. L.** (2015). Reevaluating Musculoskeletal Linkages in Suction-Feeding Fishes with X-Ray Reconstruction of Moving Morphology (XROMM). *Integr. Comp. Biol.* **55**, 36–47.
- Camp, A. L., Roberts, T. J. and Brainerd, E. L.** (2015). Swimming muscles power suction feeding in largemouth bass. *Proc. Natl. Acad. Sci.* **112**, 8690–8695.
- Camp, A. L., Roberts, T. J. and Brainerd, E. L.** (2018). Bluegill sunfish use high power outputs from axial muscles to generate powerful suction-feeding strikes. *J. Exp. Biol.* **221**,.
- Camp, A. L., Olsen, A. M., Hernandez, L. P. and Brainerd, E. L.** (2020). Fishes can use axial muscles as anchors or motors for powerful suction feeding. *J. Exp. Biol.* **223**,.
- Coates, M.** (2017). Plenty of fish in the tree. *Nature* **549**, 167–169.
- Gidmark, N. J., Taylor, C., Lopresti, E. and Brainerd, E. L.** (2015). Functional morphology of durophagy in black carp, *Mylopharyngodon piceus*. *J. Morphol.* **276**, 1422–1432.
- Giles, S., Xu, G. H., Near, T. J. and Friedman, M.** (2017). Early members of “living fossil” lineage imply later origin of modern ray-finned fishes. *Nature* **549**, 265–268.
- Grood, E. S. and Suntay, W. J.** (1983). A joint coordinate system for the clinical description of three-dimensional motions: Application to the knee. *J. Biomech. Eng.* **105**, 136–144.
- Grubich, J. R.** (2001). Prey capture in actinopterygian fishes: A review of suction feeding motor patterns with new evidence from an elopomorph fish, *megalops atlanticus*. *Am. Zool.* **41**, 1258–1265.
- Holzman, R., Day, S. W., Mehta, R. S. and Wainwright, P. C.** (2008). Integrating the determinants of suction feeding performance in centrarchid fishes. *J. Exp. Biol.* **211**, 3296–3305.
- Iriarte-Diaz, J., Terhune, C. E., Taylor, A. B. and Ross, C. F.** (2017). Functional correlates of the position of the axis of rotation of the mandible during chewing in non-human primates ☆. *Zoology* **124**, 106–118.
- Jacobs, C. N. and Holzman, R.** (2018). Conserved spatio-temporal patterns of suction-feeding flows across aquatic vertebrates: A comparative flow visualization study. *J. Exp. Biol.* **221**,.
- Kane, E. A. and Higham, T. E.** (2014). Modelled three-dimensional suction accuracy predicts prey capture success in three species of centrarchid fishes. *J. R. Soc. Interface* **11**,.
- Knorlein, B. J., Baier, D. B., Gatesy, S. M., Laurence-Chasen, J. D. and Brainerd, E. L.** (2016). Validation of XMALab software for Marker-based XROMM. *J. Exp. Biol.* **219**, 3701–3711.
- Lacepède, B.** (1803). Histoire naturelle des poissons. **5**, 1–803.

- Lauder, G. V.** (1980). Evolution of the feeding mechanism in primitive actinopterygian fishes: A functional anatomical analysis of *Polypterus*, *Lepisosteus*, and *Amia*. *J. Morphol.* **163**, 283–317.
- Lauder, G. V.** (1982). Patterns of Evolution in the Feeding Mechanism of Actinopterygian Fishes. *Am. Soc. Zool.* **285**, 275–285.
- Lauder, G. V.** (1985). Aquatic feeding in lower vertebrates. In *Functional vertebrate morphology*, pp. 210–229.
- Lemberg, J. B., Shubin, N. H. and Westneat, M. W.** (2019). Feeding kinematics and morphology of the alligator gar (*Atractosteus spatula*, Lacépède, 1803). *J. Morphol.* **280**, 1548–1570.
- Lemberg, J. B., Daeschler, E. B. and Shubin, N. H.** (2021). The feeding system of *Tiktaalik roseae*: an intermediate between suction feeding and biting. *Proc. Natl. Acad. Sci. U. S. A.* **118**, 1–10.
- Liem, K. F.** (1980). Adaptive significance of intra-and interspecific differences in the feeding repertoires of cichlid fishes. *Am. Zool.* **20**, 295–314.
- Lomax, J. J., Martinson, T. F., Jimenez, Y. E. and Brainerd, E. L.** (2020). Bifunctional Role of the Sternohyoideus Muscle During Suction Feeding in Striped Surfperch, *Embiotoca lateralis*. *Integr. Org. Biol.* **2**,.
- Manafzadeh, A. R. and Gatesy, S. M.** (2020). A coordinate-system-independent method for comparing joint rotational mobilities. *J. Exp. Biol.* **223**,.
- Markey, M. J.** (2006). In vivo cranial suture function and suture morphology in the extant fish *Polypterus*: implications for inferring skull function in living and fossil fish. *J. Exp. Biol.* **209**, 2085–2102.
- Markey, M. J. and Marshall, C. R.** (2007). Terrestrial-style feeding in a very early aquatic tetrapod is supported by evidence from experimental analysis of suture morphology. *Proc. Natl. Acad. Sci. U. S. A.* **104**, 7134–7138.
- Michel, K. B., Heiss, E., Aerts, P. and van Wassenbergh, S.** (2015). A fish that uses its hydrodynamic tongue to feed on land. *Proc. R. Soc. B Biol. Sci.* **282**,.
- Muller, M. and Osse, J. W. M.** (1984). Hydrodynamics of suction feeding in fish. *Trans. Zool. Soc. London* **37**, 51–135.
- Muller, M., Osse, J. W. M. and Verhagen, J. H. G.** (1982). A quantitative hydrodynamical model of suction feeding in fish. *J. Theor. Biol.* **95**, 49–79.
- Olsen, A. M.** (2019). A mobility-based classification of closed kinematic chains in biomechanics and implications for motor control. *J. Exp. Biol.* **222**,.
- Olsen, A. M., Camp, A. L. and Brainerd, E. L.** (2017). The opercular mouth-opening mechanism of largemouth bass functions as a 3D four-bar linkage with three degrees of freedom. *J. Exp. Biol.* **220**, 4612–4623.
- Olsen, A. M., Hernández, L. P., Camp, A. L. and Brainerd, E. L.** (2019). Channel catfish use higher coordination to capture prey than to swallow. *Proc. R. Soc. B Biol. Sci.* **286**,.
- Sanford, C. P.** (2001). Kinematic analysis of a novel feeding mechanism in the brook trout *Salvelinus fontinalis* (Teleostei: Salmonidae): behavioral modulation of a functional novelty. *J. Exp. Biol.* **204**, 3905–16.

- Tchernavin, V. V.** (1948). On the mechanical working of the head of bony fishes. *Proc. Zool. Soc. London* **118**, 129–143.
- Team, R. C.** (2019). R: A language and environment for statistical computing.
- Van Wassenbergh, S. and Aerts, P.** (2009). Aquatic suction feeding dynamics: Insights from computational modelling. *J. R. Soc. Interface* **6**, 149–158.
- Van Wassenbergh, S., Herrel, A., Adriaens, D. and Aerts, P.** (2005). A test of mouth-opening and hyoid-depression mechanisms during prey capture in a catfish using high-speed cineradiography. *J. Exp. Biol.* **208**, 4627–4639.
- Van Wassenbergh, S., Herrel, A., Adriaens, D. and Aerts, P.** (2007). Interspecific Variation in Sternohyoideus Muscle Morphology in Clariid Catfishes: Functional Implications for Suction Feeding. *J. Morphol.* **268**, 232–242.
- Vereijken, B., van Emmerik, R., Whiting, H. T. A. and Newell, K. M.** (1992). Free(z)ing degrees of freedom in skill acquisition. *J. Mot. Behav.* **24**, 133–142.
- Wainwright, P. C. and Day, S. W.** (2007). The forces exerted by aquatic suction feeders on their prey. *J. R. Soc. Interface* **4**, 553–560.
- Westneat, M. W. and Wainwright, P. C.** (1989). Feeding mechanism of *Epibulus insidiator* (Labridae; Telesotei): evolution of a novel functional system. *J. Morphol.* **205**, 269–275.

## Figures

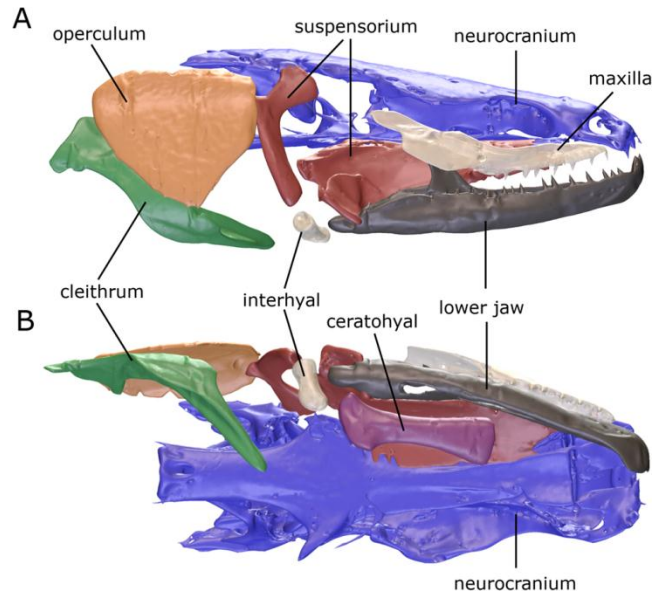


**Fig. 1. Cranial skeletal anatomy of *P. bichir*.** Rigid bodies measured and linkage-central bones in the skull and cleithrum from two views: (A) lateral and (B) ventral. Colored bones are rigid bodies animated in this study, while pale bones (interhyal and maxilla) are shown for context but were not animated.

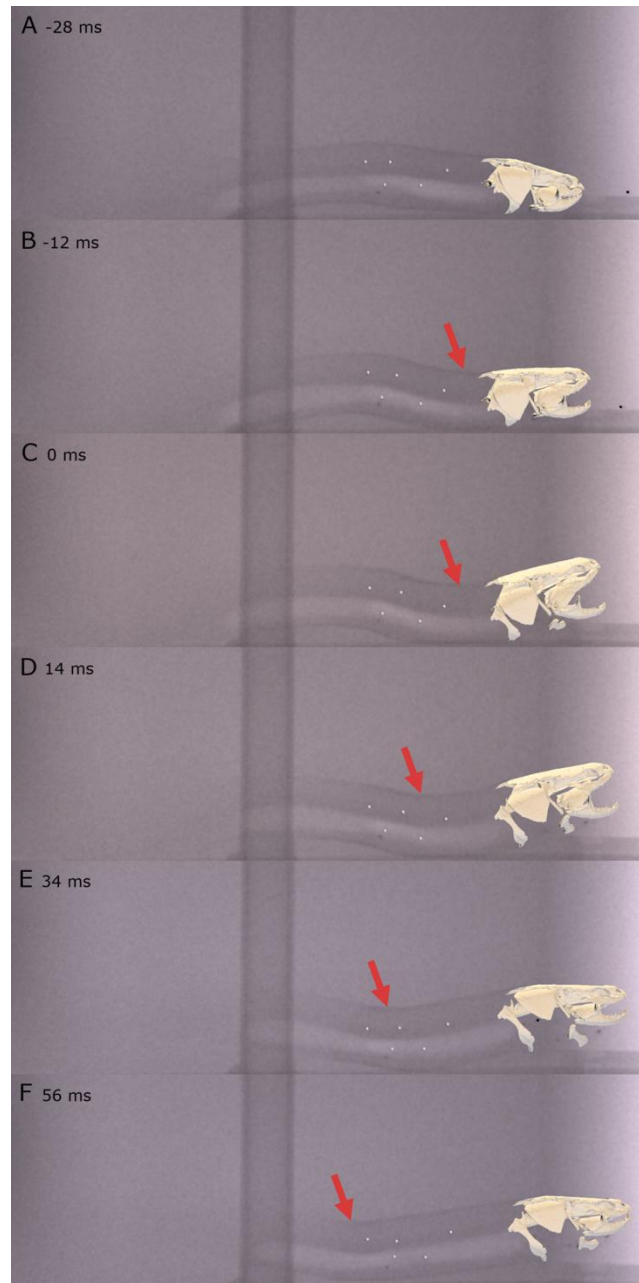


**Fig. 2. Still frame sequence of X-Ray video and corresponding XROMM animation.** Skull and body postures in 6 frames: (A) just prior to motion onset (-28 ms), (B) halfway between motion onset and maximum gape (-12 ms), (C) maximum gape (0 ms), (D) early in compressive phase (14 ms), (E) midway through compressive phase (34 ms), (F) mouth closed (56 ms). The black sphere visible in (A) (B) and (E) overlays a 1 mm marker implanted in the feeder fish. White spheres overlay markers used to animate body plane. Red arrows highlight a posteriorly traveling wave of vertebral bending.

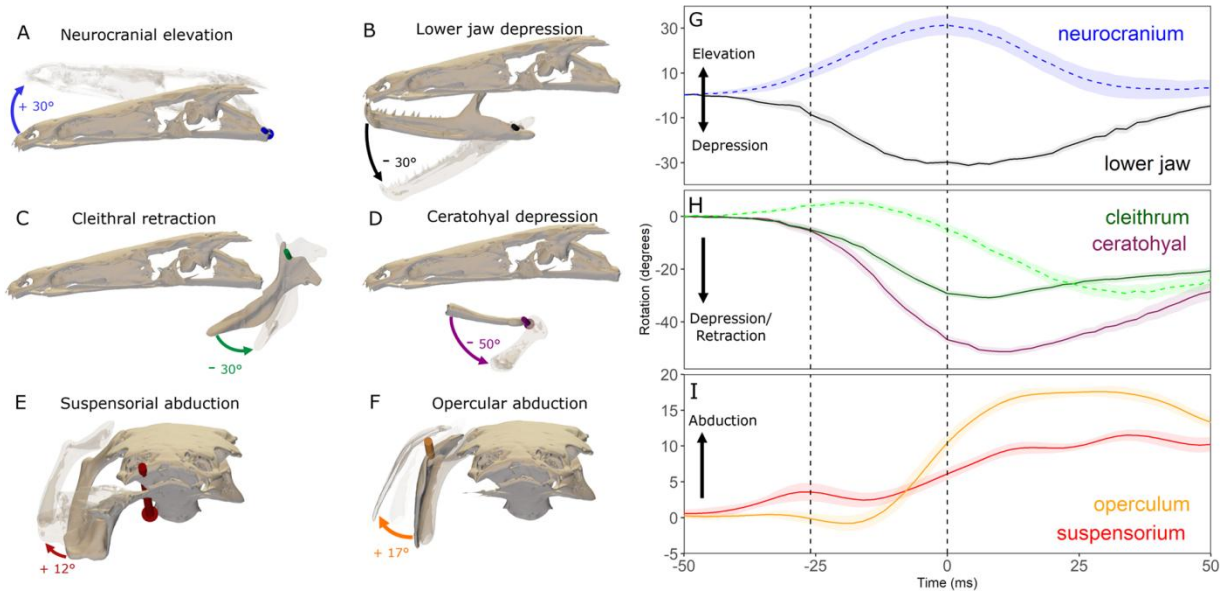


**Fig. 3. Mean rotations of largest magnitude axes for anatomically-oriented JCSs.** (A-F) Z-axes for each anatomically-oriented JCS used to measure the primary motion captured for each bone in lateral single-camera studies. Colors correspond to kinematic traces shown in G-I, and the value listed is the highest mean rotation. (A) Neurocranial elevation, medial view. (B) Lower jaw depression, medial. (C) Cleithral retraction (rotation about a mediolateral axis), medial. (D) Ceratohyal depression, medial. (E) Suspensorial abduction (rotation about an anteroposterior axis), anterior. (F) Opercular abduction (rotation about an anteroposterior axis), anterior. (G-I) Shows mean  $\pm$  SEM of z-axis rotations (largest axis of expected rotation) of bones from all tracked strikes across three individuals (11 trials for suspensorium, 16 trials for operculum, 18 for all other variables). All rotations were zeroed to average resting position by subtracting average motion during the first 25 frames recorded. Rotations for G and H are unfiltered, rotations in panel I (suspensorial and opercular motion) were smoothed using a 50 Hz low-pass Butterworth filter. Vertical lines denote onset of prey motion (-26 ms) and peak gape (0 ms). Dashed lines (neurocranium and cleithrum) were measured relative to a body plane and solid lines were measured relative to the neurocranium.

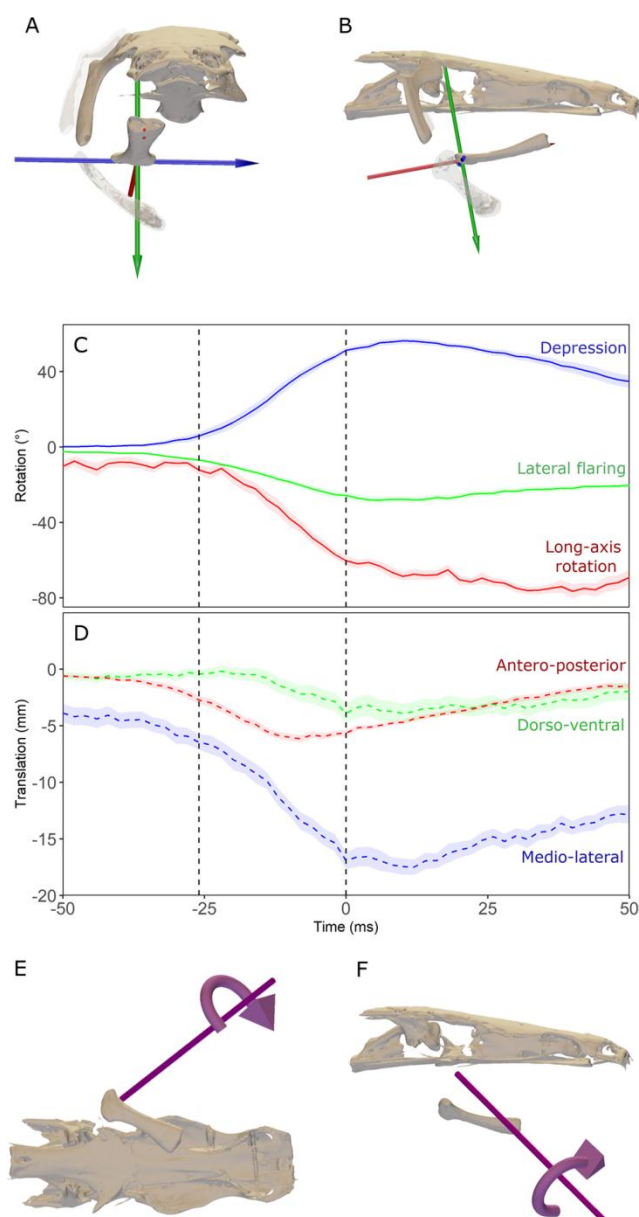


**Fig. 4. Mean 3D kinematics of the ceratohyal relative to the neurocranium measured using a joint-oriented JCS.** Panels (A) anterior and (B) lateral view show the position of the neurocranium, hyomandibula, and distal JCS at mouth closed or resting position (solid bones) and at maximum gape (transparent bones). This JCS was positioned to enable measurement of long-axis rotation of the ceratohyal. Note that the interhyal (between hyomandibula and ceratohyal, Fig. 1) is not shown here as it was not animated in this study. (C) and (D) show means  $\pm$  SEM of 18 trials across three individuals, with rotations about each axis in panel (C) (solid lines) and translations along each axis in panel (D) (dashed lines). Vertical lines denote the

onset of prey motion (-26 ms) and peak gape (0 ms). (E) and (F) show the instantaneous helical axis of the ceratohyal from a representative trial at -14 ms before peak gape, or peak ceratohyal velocity (as calculated in Fig. 6) in (E) ventral and (F) lateral view. The helical axis follows a right-hand rule designation, indicating that the ceratohyal is being depressed at this time, with the direction of rotation about the cylindrical axis shown (also see Video S2).

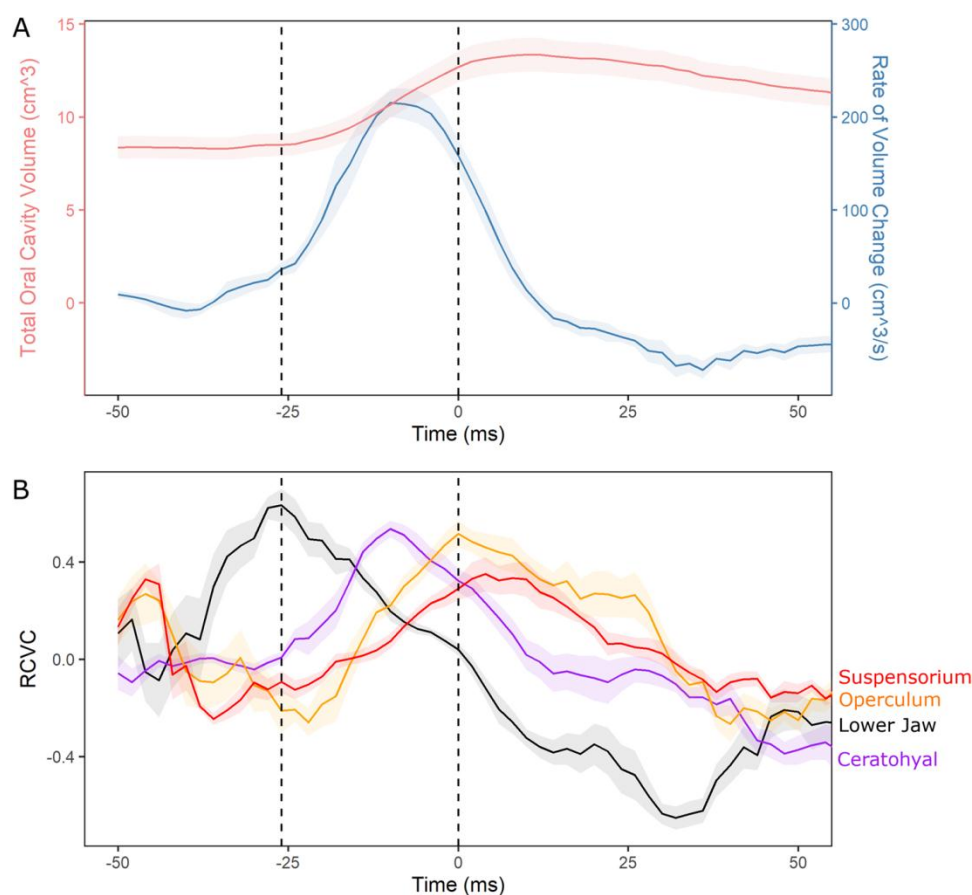


**Fig. 5. Change in oral cavity volume and relative contribution of each rigid body. (A)**

Change in oral cavity volume during feeding strikes. Total volume (salmon-colored line) was calculated directly from the endocast, while rate of volume change (blue line) was calculated as the derivative of total volume, or the volume change from one frame to the next. (B) Relative contribution to volume change (RCVC) of each rigid body or skeletal element to summed delta volume. Each line is a ratio of that bone's contribution to the summed or absolute delta volume (see Methods for details). Lines show mean  $\pm$  SEM of strikes across two individuals (7 trials for suspensorium, 11 trials for operculum, 13 for all other variables). Vertical lines denote onset of prey motion (-26 ms) and peak gape (0 ms).

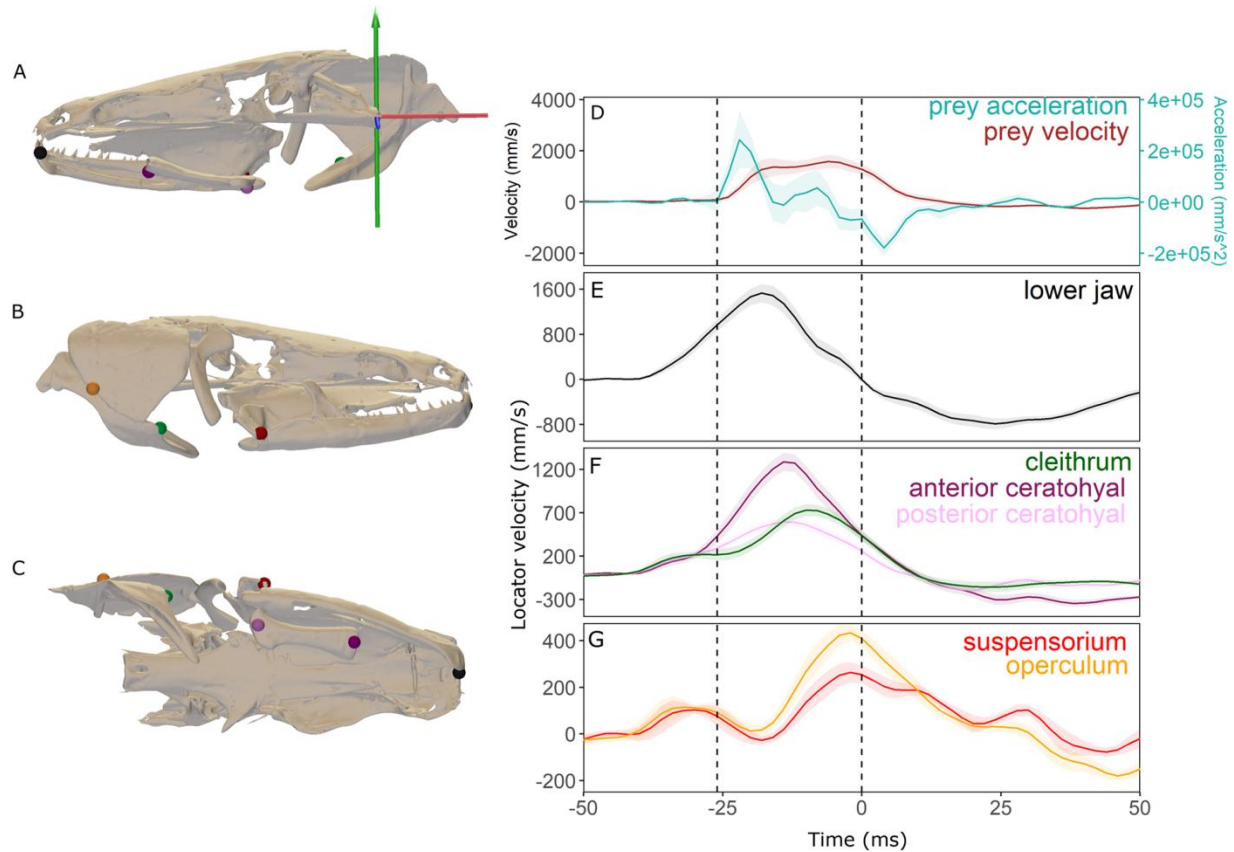
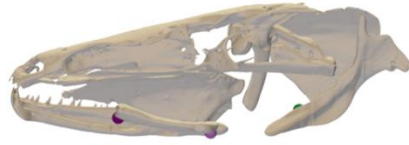


**Fig. 6. Mean displacement velocity of bone points of interest.** (A-C) Locators for each bone used to measure the point undergoing the highest degree of motion during a strike. Colors correspond to kinematic traces shown in E-G. (A) Medial view with ACS coordinate system paired to the neurocranium (from which each locator's displacement velocity was calculated). (B) Lateral view. (C) Ventral view. (D-G) Mean  $\pm$  SEM of all successful strikes across three individuals (9 trials for suspensorium, 14 trials for operculum, 16 for all other variables). Prey data and rotations are unfiltered, except for suspensorial and opercular motion, which were smoothed using a 50 Hz low-pass Butterworth filter. Vertical lines denote onset of prey motion (-26 ms) and peak gape (0 ms). (D) Prey velocity and acceleration in world space. Panels (E-G) show locator displacements for each bone of interest, all measured relative to the neurocranium.

A



B

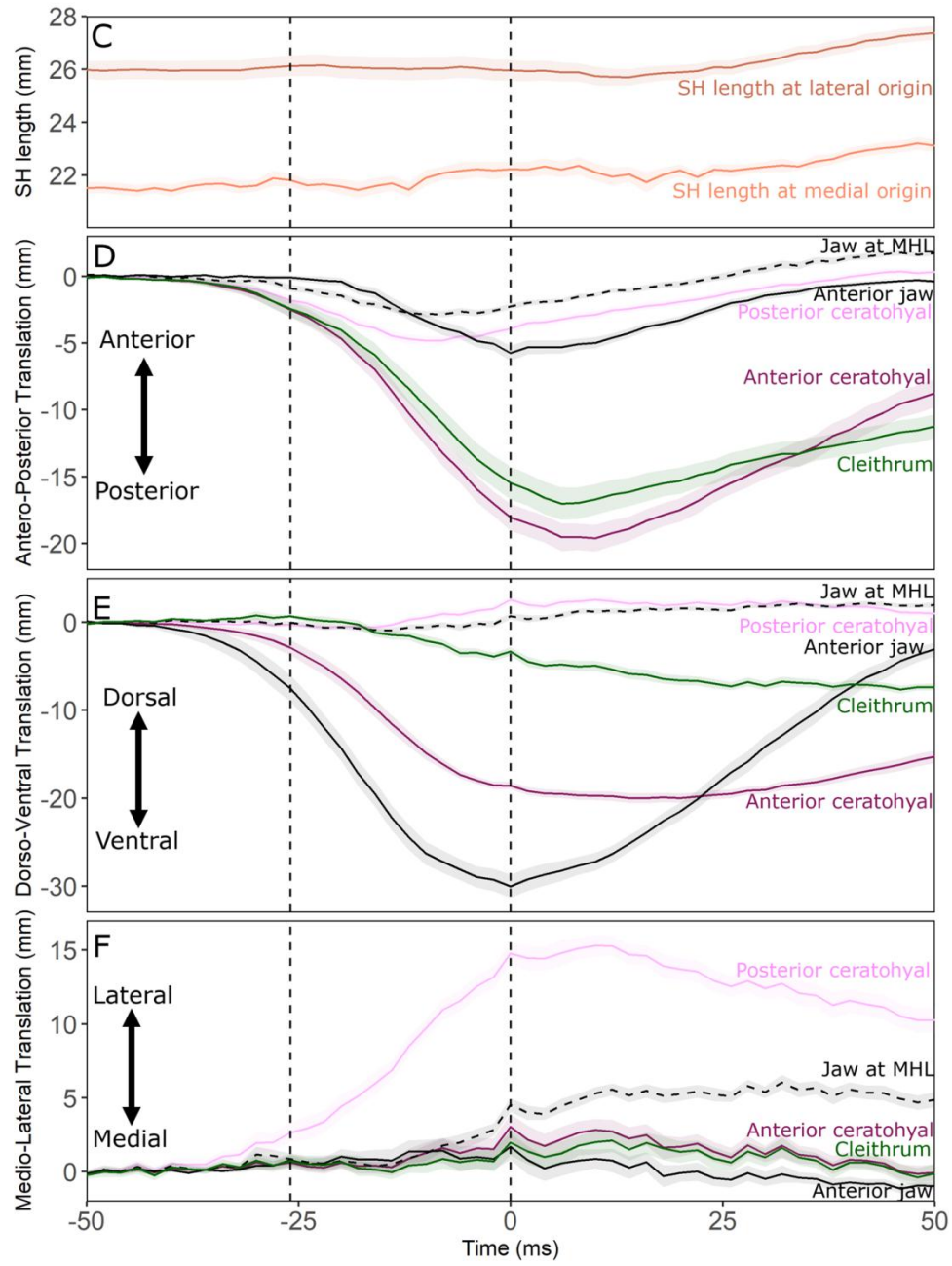
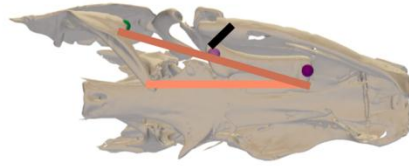


**Fig. 7. Sternohyoideus length and translations of key points on cleithrum, ceratohyal, and lower jaw.** (A) Medial view of the skull showing locators measured for anterior ceratohyal (dark purple), posterior ceratohyal (light purple), and ventrolateral cleithrum (green). (B) Ventral view of the skull showing locators measured and orientation of the lateral-most sternohyoideus (SH) origin (dark orange bar), medial-most SH origin (light orange bar), and mandibulohyoid ligament (black bar). (C) Length of sternohyoideus muscle from each origination point (to a single insertion point) across strikes, measured as the distance between origin and insertion points on the cleithrum and ceratohyal. (D-F) Translations of the lower jaw attachment of the MHL, anterior and posterior ceratohyal, and ventrolateral cleithrum in an anteroposterior (D), dorsoventral (E), and mediolateral (F) axis, all measured relative to the neurocranium using the same ACS as shown in Fig. 6. All lines in C-F show mean  $\pm$  SEM of all tracked strikes across three individuals (18 trials). Vertical lines denote onset of prey motion (-26 ms) and peak gape (0 ms).

**Table 1.** Mean peak magnitude and time to peak for bone locator velocity and maximum cross-correlation and lag times between each bone velocity and prey acceleration (trace data shown in Fig. 6).

Bone Locator	Number of trials	Peak velocity (mm s <sup>-1</sup> )	Time to peak velocity (ms)	Maximum cross-correlation (R)	Lag at max cross-corr (ms)
Ceratohyal anterior	(n=16)	1560 $\pm$ 80.8	-14.3 $\pm$ 1.24	0.302	6
Ceratohyal posterior	(n = 16)	709 $\pm$ 42.7	-14.8 $\pm$ 1.80	0.26	8
Lower Jaw	(n = 16)	1918 $\pm$ 92.1	-16.9 $\pm$ 1.44	0.303	2
Operculum	(n = 14)	568 $\pm$ 40.1	-1.3 $\pm$ 3.83	0.219	20
Suspensorium	(n = 9)	414 $\pm$ 45.0	0.4 $\pm$ 6.14	0.101	34

**Table 2.** Absolute delta volume and bone RCVC magnitudes at overall peaks, time of maximum total volume, and time at maximum delta volume (trace data shown in Fig. 5).

	Absolute Delta Volume (cm <sup>3</sup> freeze interval <sup>-1</sup> )		Lower Jaw RCVC		Ceratohyal RCVC		Operculum RCVC		Suspensorium RCVC	
Peak magnitude	2.3	± 0.167	0.77	± 0.033	0.61	± 0.035	0.63	± 0.063	0.48	± 0.093
Time at peak	-10.9	± 1.00	-26.3	± 1.34	-4.6	± 3.17	10.0	± 3.50	5.4	± 1.84
Magnitude at peak total volume	0.45	± 0.067	0.25	± 0.026	0.51	± 0.030	0.22	± 0.027	0.07	± 0.030
Magnitude at peak delta volume	-	-	-0.36	± 0.049	0.05	± 0.061	0.40	± 0.076	0.20	± 0.035

**Table 3.** Peak cross-correlations and lag times between elements involved in lower jaw opening linkage, abbreviations are as follows: AP = anteroposterior, DV = dorsoventral, ML = mediolateral, with locators the same as shown in Fig. 6.

Link Responsible	Lead Variable	Lag Variable	Max Cross- Correlation		Lag time (ms)	
Sternohyoideus directly	Cleithrum AP	Anterior Ceratohyal AP	0.95	± 0.01	1.00	± 0.40
		Anterior Ceratohyal DV	0.94	± 0.01	0.22	± 0.22
Sternohyoideus indirectly	Cleithrum AP	Posterior Ceratohyal AP	0.63	± 0.03	9.00	± 5.54
		Posterior Ceratohyal DV	0.45	± 0.02	-38.33	± 9.24
MHL directly	MHL Jaw AP	Posterior Ceratohyal AP	0.91	± 0.01	0.00	± 0.00
		Posterior Ceratohyal DV	0.69	± 0.03	-10.89	± 6.60
	MHL Jaw DV	Posterior Ceratohyal AP	0.60	± 0.03	6.11	± 4.66
		Posterior Ceratohyal DV	0.77	± 0.03	-7.11	± 2.11
	MHL Jaw ML	Posterior Ceratohyal AP	0.55	± 0.03	-17.89	± 6.15
		Posterior Ceratohyal DV	0.43	± 0.02	25.33	± 10.77
MHL indirectly	Anterior Jaw DV	Anterior Ceratohyal AP	0.86	± 0.01	5.11	± 0.69
		Anterior Ceratohyal DV	0.77	± 0.02	5.78	± 0.62
		Posterior Ceratohyal AP	0.87	± 0.01	-2.67	± 0.40
		Posterior Ceratohyal DV	0.55	± 0.03	-9.56	± 9.58
Both	Cleithrum AP	Anterior Jaw DV	0.80	± 0.02	7.67	± 1.27

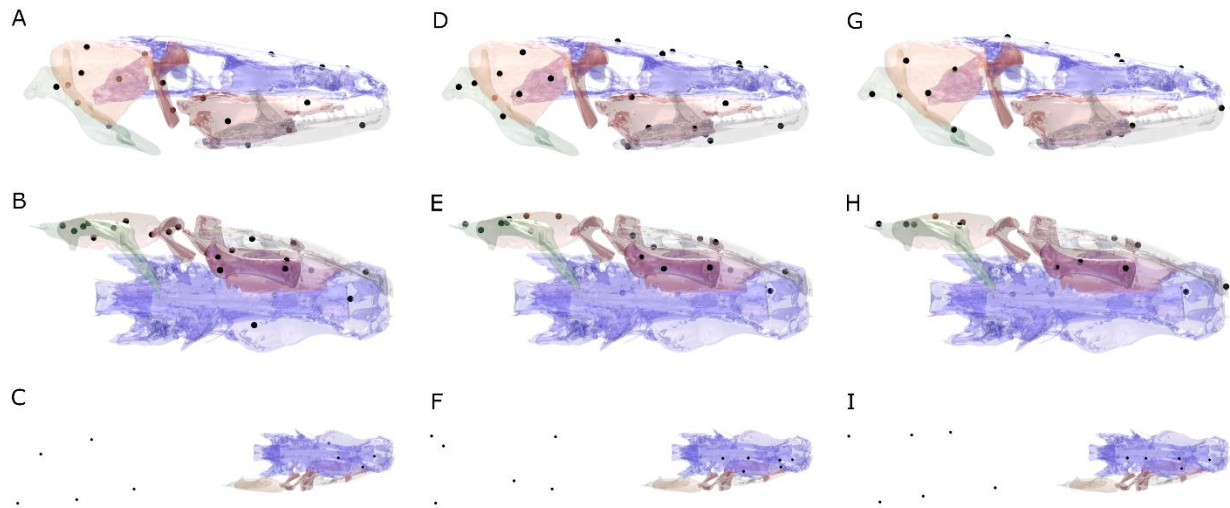


**Fig. S1.** Marker implant sites for all individuals, superimposed on P3 CT scan. A-C) P1 A) Lateral B) Ventral and C) Dorsal view. D-F) P2 D) Lateral E) Ventral and F) Dorsal view. G-I) P1 G) Lateral H) Ventral and I) Dorsal view. In C, F, I) all markers except Neurocranial and Body Plane are hidden for clarity.

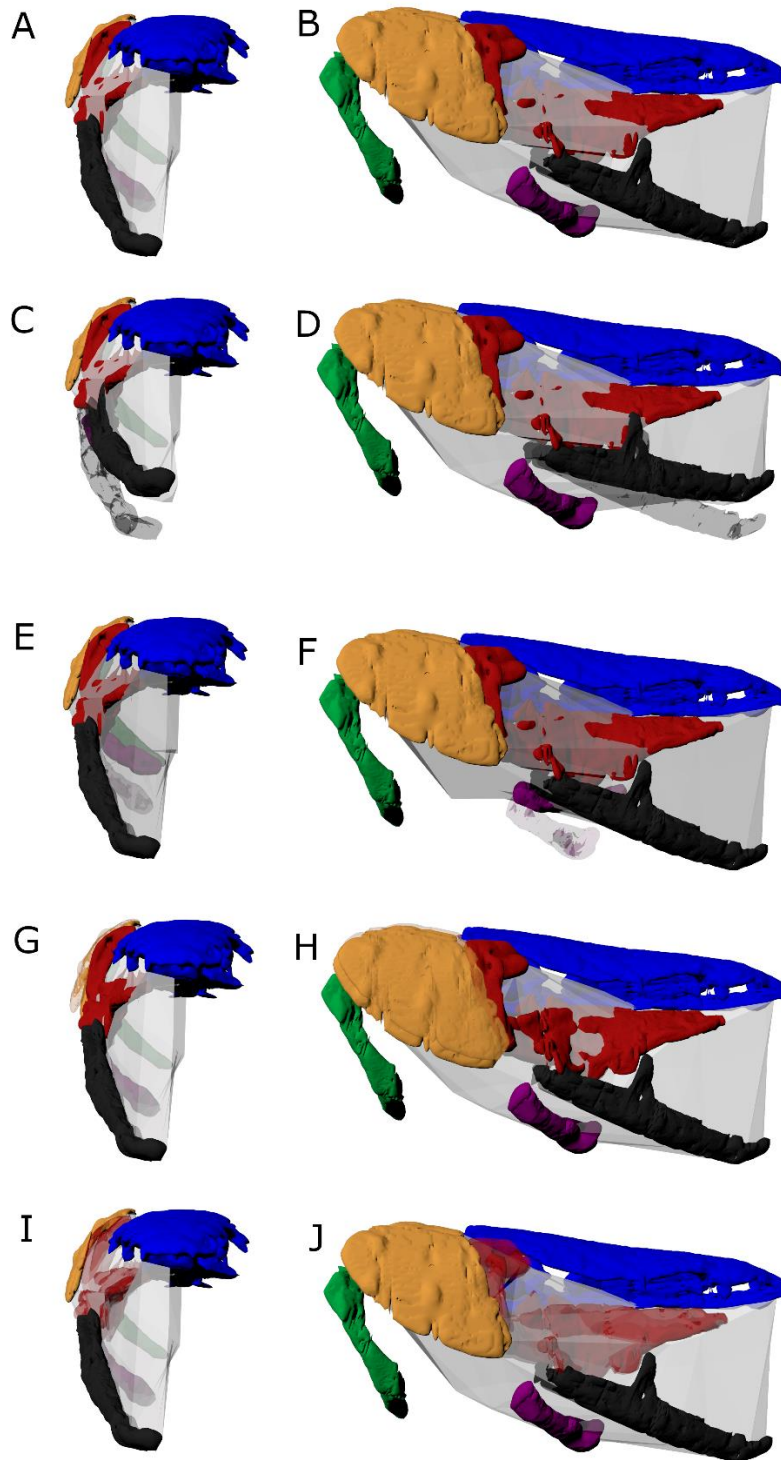


**Fig. S2.** Oral cavity volume endocast alpha hulls at maximum gape, anterior and lateral views. A & B) Reference volume, all bones unfrozen. C-J) “Frozen” volumes, with solid bone at frozen position (held to neurocranium from 5 frames prior) and transparent bone at reference position for: jaw (C & D) ceratohyal (E & F) operculum (G & H), and suspensorium (I & J).

**Table S1.** Precision information from *in vivo* co-osseous pairs of intermarker distances.

<b>P1</b> Collected at UC	Standard deviations of pairwise intermarker distances within each rigid body			
	Min	Max	Mean	SEM
Body Plane	0.16	2.734	0.76	0.086
Ceratohyal	0.075	0.236	0.13	0.008
Cleithrum	0.071	0.115	0.088	0.003
Lower Jaw	0.086	0.125	0.099	0.003
Neurocranium	0.078	0.119	0.094	0.002
Operculum	0.069	0.123	0.096	0.002
Suspensorium	0.07	0.149	0.112	0.003

<b>P1</b> Collected at Brown	Standard deviations of pairwise intermarker distances within each rigid body			
	Min	Max	Mean	SEM
Body Plane	0.07	0.848	0.251	0.046
Ceratohyal	0.04	0.104	0.062	0.006
Cleithrum	0.04	0.049	0.044	0.002
Lower Jaw	0.051	0.068	0.058	0.003
Neurocranium	0.042	0.131	0.069	0.006
Operculum	0.038	0.041	0.039	0.002
Suspensorium	0.04	0.106	0.068	0.007

<b>P2</b>	Standard deviations of pairwise intermarker distances within each rigid body			
	Min	Max	Mean	SEM
Body Plane	0.145	2.184	0.604	0.063
Ceratohyal	0.090	0.174	0.125	0.007
Cleithrum	0.086	0.188	0.121	0.005
Lower Jaw	0.107	0.209	0.155	0.010
Neurocranium	0.092	0.194	0.123	0.003
Operculum	0.086	0.131	0.112	0.003
Suspensorium	0.093	0.171	0.122	0.013

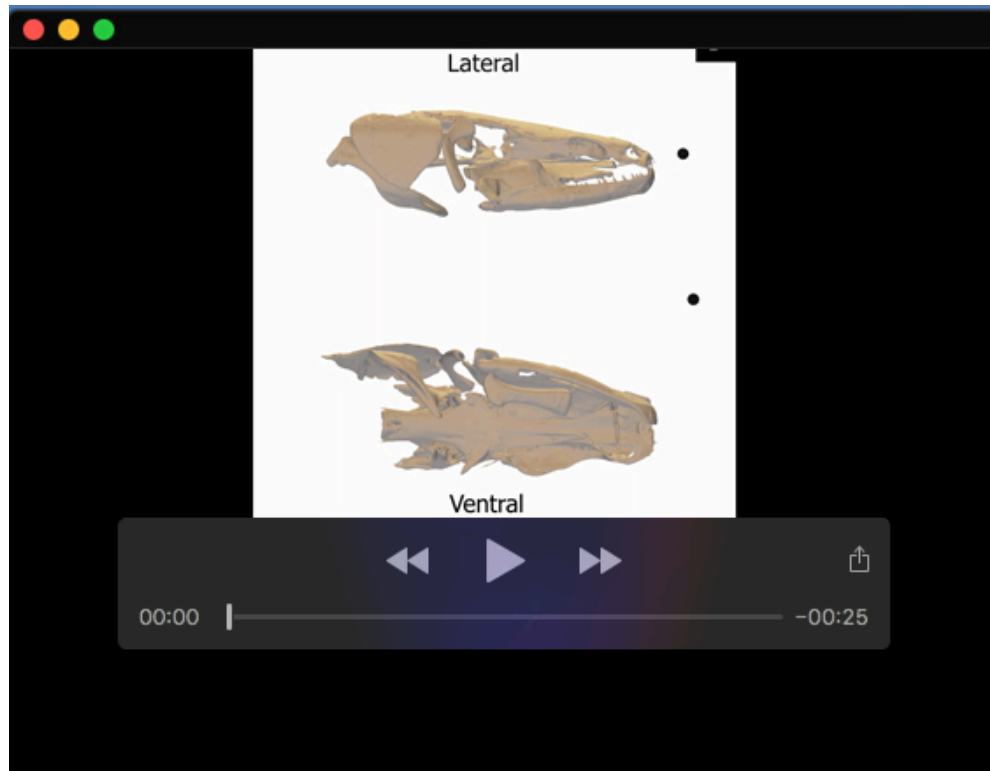
<b>P3</b>	Standard deviations of pairwise intermarker distances within each rigid body			
	Min	Max	Mean	SEM
Body Plane	0.118	2.061	0.5	0.036
Ceratohyal	0.086	0.125	0.102	0.002
Cleithrum	0.08	0.114	0.094	0.002
Lower Jaw	0.086	0.134	0.107	0.003
Neurocranium	0.079	0.271	0.144	0.007
Operculum	0.074	0.123	0.095	0.003

**Table S2.** Mean peak magnitude and time to peak for z-axis rotation values.

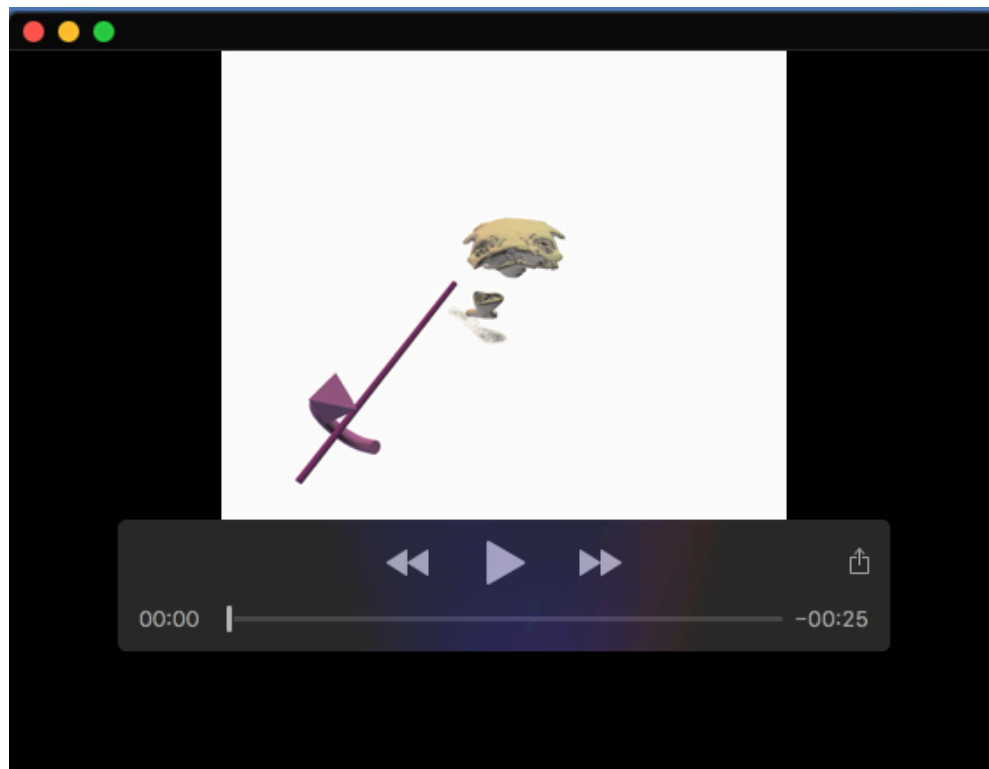
Bone	Number of Trials	Maximum Z axis rotation (°)			Time to peak Z rotation (ms)		
Ceratothyal	(n = 18)	-55.3	±	1.55	14.1	±	3.01
Lower Jaw	(n = 18)	-34.0	±	0.79	3.7	±	1.98
Cleithrum	(n = 18)	-32.4	±	0.97	10.7	±	3.00
Neurocranium	(n = 18)	33.6	±	4.67	5.0	±	5.24
Opreculum	(n = 16)	19.1	±	1.00	24.6	±	2.17
Suspensorium	(n = 11)	12.8	±	1.10	30.9	±	6.60

**Table S3.** Mean magnitudes and timing of peak x, y, and z translations of anterior and posterior ceratothyal, lateral cleithrum, and jaw at mandibulohyoid ligament across trials, with translations calculated as in Fig. 7 but averaged the peak from each trial rather than by time point.

Bone	Translation Max/Min	Magnitude (mm)			Timing (ms)		
<b>Anterior Ceratothyal</b>	Peak Anterior	0.2	±	0.06	-44.3	±	1.36
	Peak Posterior	-20.5	±	1.02	11.7	±	1.91
	Peak Dorsal	0.2	±	0.05	-39.2	±	1.66
	Peak Ventral	-20.7	±	0.57	15.7	±	3.03
	Peak Lateral	4.9	±	0.67	1.6	±	4.27
	Peak Medial	-2.3	±	0.44	-5.4	±	7.54
<b>Posterior Ceratothyal</b>	Peak Anterior	0.9	±	0.15	18.9	±	9.79
	Peak Posterior	-5.5	±	0.39	-11.3	±	1.42
	Peak Dorsal	3.9	±	0.34	20.0	±	3.28
	Peak Ventral	-1.5	±	0.26	-16.8	±	5.37
	Peak Lateral	16.3	±	0.70	9.2	±	1.73
	Peak Medial	-1.0	±	0.17	-41.3	±	1.84
<b>Cleithrum</b>	Peak Anterior	0.4	±	0.14	-42.0	±	1.53
	Peak Posterior	-18.4	±	1.18	14.7	±	3.70
	Peak Dorsal	2.1	±	0.39	-31.8	±	2.14
	Peak Ventral	-8.5	±	0.43	36.7	±	2.43
	Peak Lateral	4.6	±	0.58	3.8	±	5.93
	Peak Medial	-3.1	±	0.47	2.9	±	8.00
<b>Jaw at MHL</b>	Peak Anterior	2.1	±	0.20	41.8	±	4.31
	Peak Posterior	-3.5	±	0.23	-9.0	±	1.48
	Peak Dorsal	3.2	±	0.27	32.2	±	5.06
	Peak Ventral	-2.0	±	0.27	-14.6	±	3.39
	Peak Lateral	7.3	±	0.43	24.7	±	3.74
	Peak Medial	-1.8	±	0.29	-27.9	±	3.70



**Movie 1.** Lateral and ventral views of representative *P. bichir* feeding strike, with prey marker animated. The exported camera view is frozen to the neurocranium. See supplemental information page for link to video.



**Movie 2.** Rotating view of helical axis of rotation described for *P. bichir* ceratohyal rotation, as calculated in Fig. 4. See supplemental information page for link to video.